Astronomy & Astrophysics

Arcsecond resolution images of the chemical structure of the low-mass protostar IRAS 16293-2422

An overview of a large molecular line survey from the Submillimeter Array*

J. K. Jørgensen[1,2], T. L. Bourke[3], Q. Nguyễn Lương[4,5], and S. Takakuwa[6]

[1] Centre for Star and Planet Formation, Niels Bohr Institute, University of Copenhagen, Juliane Maries Vej 30, 2100 Copenhagen Ø., Denmark
e-mail: jeskj@nbi.dk
[2] Natural History Museum of Denmark, University of Copenhagen, Øster Voldgade 5-7, 1350 Copenhagen K., Denmark
[3] Harvard-Smithsonian Center for Astrophysics, 60 Garden Street MS42, Cambridge, MA 02138, USA
[4] Laboratoire AIM, CEA/DSM, IRFU/Service d'Astrophysique, 91191 Gif-sur-Yvette Cedex, France
[5] Argelander Institute for Astronomy, University of Bonn, Auf dem Hügel 71, 53121 Bonn, Germany
[6] Academia Sinica Institute of Astronomy and Astrophysics, PO Box 23-141, Taipei 10617, Taiwan

ABSTRACT

It remains a key challenge to establish the molecular content of different components of low-mass protostars, like their envelopes and disks, and how this depends on the evolutionary stage and/or environment of the young stars. Observations at submillimeter wavelengths provide a direct possibility to study the chemical composition of low-mass protostars through transitions probing temperatures up to a few hundred K in the gas surrounding these sources. This paper presents a large molecular line survey of the deeply embedded protostellar binary IRAS 16293-2422 from the Submillimeter Array (SMA) – including images of individual lines down to $\approx 1.5-3''$ (190−380 AU) resolution. More than 500 individual transitions are identified related to 54 molecular species (including isotopologues) probing temperatures up to about 550 K. Strong chemical differences are found between the two components in the protostellar system with a separation between, in particular, the sulfur- and nitrogen-bearing species and oxygen-bearing complex organics. The action of protostellar outflow on the ambient envelope material is seen in images of CO and SiO and appear to influence a number of other species, including (deuterated) water, HDO. The effects of cold gas-phase chemistry is directly imaged through maps of CO, N_2D^+ and DCO^+, showing enhancements of first DCO^+ and subsequently N_2D^+ in the outer envelope where CO freezes-out on dust grains.

Key words. circumstellar matter – ISM: molecules – stars: formation – ISM: jets and outflows – submillimeter: ISM – ISM: individual objects: IRAS 16293-2422

1. Introduction

Developing the understanding of the chemical structure and evolution of star-forming regions remains an important task. Understanding the molecular composition of protostars and, in particular, the innermost regions of the circumstellar envelopes and disks relates to some of the key scientific questions concerning star and planet formation, for example, what level of chemical complexity can arise around protostars (e.g., van Dishoeck & Blake 1998; Ceccarelli et al. 2007; Herbst & van Dishoeck 2009). Also, for studying the physics of the star formation process, it is desired to know which molecular species are tracing specific components of young stellar objects, such as their envelope, disks etc. This paper presents the results of a large Submillimeter Array (SMA) survey of the molecular line emission on few hundred AU scales toward the deeply embedded low-mass protostar IRAS 16293-2422 and discusses some of the signatures of the physics and chemistry occurring in this deeply embedded protobinary system.

IRAS 16293-2422 has long been considered one of the "template" sources for astrochemistry. Being the deeply embedded (Class 0) low-mass protostar with the richest line spectrum, it has been the subject of many targeted (sub)millimeter wave spectroscopic studies (e.g., Blake et al. 1994; van Dishoeck et al. 1995; Ceccarelli et al. 1998, 2000; Cazaux et al. 2003; Caux et al. 2011) as well as specialized modeling efforts attempting to establish its chemical composition – in particular, variation in its molecular abundances as function of radius (e.g., Ceccarelli et al. 2000; Schöier et al. 2002). The detections of complex organics toward this source (e.g., Cazaux et al. 2003; Bottinelli et al. 2004; Kuan et al. 2004; Bisschop et al. 2008) have sparked new interest in the physical processes that can lead to the evaporation of icy grain mantles on small scales of protostars – and thereby also the chemical processes determining their molecular compositions.

However, IRAS 16293-2422 has also illustrated some of the inherent difficulties in relating the larger scale line emission picked up by single-dish telescopes to the source structures on few hundred AU scales, e.g., revealed by millimeter interferometric observations. After the identification of IRAS 16293-2422 as a binary through high resolution centimeter

---

and millimeter wavelength continuum observations (Wootten 1989; Mundy et al. 1992), it has been the target of many studies trying to relate the structure of the two main components to their line emission and place them in an evolutionary context. The southeastern of the two components, "IRAS 16293A", appears resolved in continuum observations, breaking into a number of different components at subarcsecond scales (Chandler et al. 2005; Pech et al. 2010). The northwestern component, "IRAS 16293B", in contrast appears unresolved on these scales. In terms of line emission the two sources also show significant differences: both show detection of complex organic molecules for example (Bottinelli et al. 2004; Kuan et al. 2004; Remijan & Hollis 2006; Bisschop et al. 2008) – but the relative line strengths and widths vary between the two sources. Whereas it is generally agreed that the IRAS 16293A component is protostellar in nature – it has been suggested that the IRAS 16293B component either represented a more evolved (T Tauri) star (e.g., Stark et al. 2004; Takakuwa et al. 2007) or alternatively a very young object, possibly before starting accretion/mass loss (Chandler et al. 2005).

In this paper we present a large survey of the line emission in the 230 GHz and 345 GHz atmospheric windows of IRAS 16293-2422 from the SMA. The paper is laid out as follows: Sect. 2 describes the details of the observations and Sect. 3 presents an overview of the line emission in global terms. Section 4 discusses a few of the key aspects that can be derived from just visual inspection of the molecular line emission maps and Sect. 5 summarizes the main conclusions of the paper.

2. Observations

IRAS 16293-2422 was observed in a number of spectral settings between 2004 and 2007 using the SMA, (Ho et al. 2004). We here focus on four sets of observations covering different spectral setups at 220 and 340 GHz. The log of the observations, beam sizes and noise levels are summarized in Table 1. Previous papers by Yeh et al. (2008) and Bisschop et al. (2008) presented part of these data from 2005 Feb. 18, focusing on the CO outflow emission and selected complex organic molecules, respectively.

The data were taken with the SMA in its compact or compact-North configuration resulting in average beam sizes of $\approx 2-4''$ (250−500 AU at a typical distance to Ophiuchus of 125 pc). For three of the four datasets a pointing center at $\alpha = 16^\text{h}32^\text{m}22.91^\text{s}$, $\delta = -24^\text{d}28'35''.5$ [J2000] was used. For the last dataset (2007 March 22) the pointing center was $\alpha = 16^\text{h}32^\text{m}22.72^\text{s}$, $\delta = -24^\text{d}28'34''.3$ [J2000]. The positions for the two main continuum peaks seen in these images (Fig. 1) are at $\alpha = 16^\text{h}32^\text{m}22.87^\text{s}$, $\delta = -24^\text{d}28'36''.4$ [J2000] (IRAS16293A or "A") and $\alpha = 16^\text{h}32^\text{m}22.62^\text{s}$, $\delta=-24^\text{d}28'32''.4$ [J2000] (IRAS16293B or "B") with an agreement between the fitted positions of about 0.2''. The field of view of the SMA observations cover a region of 30−50'' (3750−6250 AU; diameter) at 345−230 GHz.

Two of the four datasets (the 220/230 GHz and 337/347 GHz datasets from 2005 February 18 and 2007 March 22, respectively) were taken as part of dual receiver observations with the high frequency receiver tuned to lines at 690 GHz. For these datasets the excellent weather conditions required for the 690 GHz observations also result in significantly improved rms noise levels in the lower frequency data discussed here. The correlator was configured with uniform spectral coverage over the (at the time) ≈ 2 GHz bandwidth in each sideband of the SMA receivers. Each 2 GHz sideband was covered by 24 chunks of the correlator with a width of 128 MHz each – and each
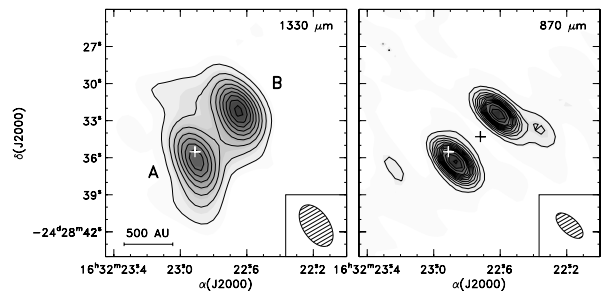
Fig. 1. Continuum images of IRAS 16293-2422 at 1.3 mm (*left*) and 0.87 mm (*right*). In the *left panel* the contours are given in steps of 0.1 Jy beam^{-1} to 1.0 Jy beam^{-1} and from there in steps of 0.2 Jy beam^{-1} and in the right in steps of 0.2 Jy beam^{-1} to 2.0 Jy beam^{-1} and from there in steps of 0.4 Jy beam^{-1} (in the continuum data the noise level is determined by the interferometer dynamic range). The white plus-signs indicate the pointing centers of the observations, except those from 2007 March 22 for which the pointing center is indicated by the black plus-sign in the *right panel*.

chunk split into 256 channels (128 channels for the dual receiver observations).

The data were calibrated using the standard recipes – including calibration of the complex gains by observations of the nearby quasar J1743-038 and flux and passband calibration by observations of planets (Uranus, in particular). The initial data reduction was performed using the MIR package (Qi 2008) and continuum subtracted line maps were created using the Miriad package (Sault et al. 1995) with which further analysis was also done.

3. Analysis

In this paper we focus on the morphology of the line emission from the IRAS 16293-2422 data and refer to other papers in the literature for a more in-depth discussion of continuum emission toward the sources. We make the data publicly available for anyone interested in a more in-depth analysis of specific molecules: the SMA raw data are available through CfA Radio Telescope Data Center[1] and the spectra toward the two continuum peaks in FITS format through a dedicated website[2] (the full reduced datacubes are available on a collaborative basis).

Figures 2–9 show the composite spectra toward the continuum positions of IRAS 16293A and IRAS 16293B. Key differences for the line emission in the two sources also noted in previous papers are clearly illustrated: typically the IRAS 16293A component show broader and stronger lines, for example, clearly illustrated in the methanol CH_3OH $J_k = 7_k - 6_k$ branch at 338.4 GHz. On the other hand, IRAS 16293B shows the presence of some sets of lines not seen in IRAS 16293A, e.g., in the frequency range from 346.9−347.3 GHz harboring a number of transitions of acetaldehyde, CH_3CHO.

A few lines show very complex profiles likely due to combinations of optical depth effects and spatial resolving out due to the interferometer's lack of short-spacings: with the shortest projected baselines of about 8 m length (Table 1) the SMA observations for example recover less than 50% of any emission with a Gaussian distribution with a *FWHM* of 10−15'' (i.e., molecules with a similar surface brightness distribution as the envelope traced by single-dish continuum observations; Schöier et al. 2002) and an even smaller fraction for molecules more

---

[1] http://cfa-www.harvard.edu/rtdc
[2] http://www.nbi.dk/~jeskj/sma-iras16293.html
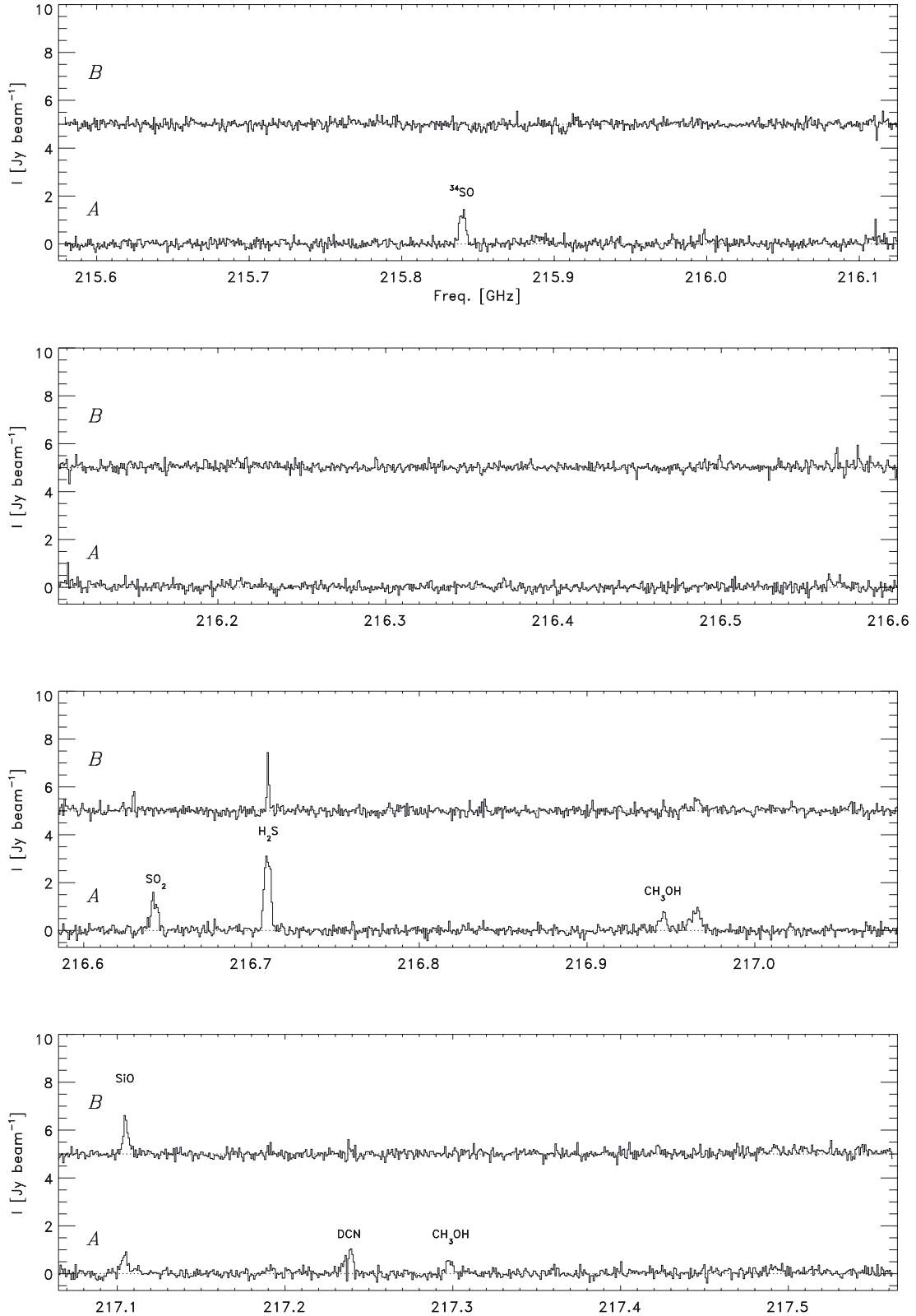
Fig. 2. Composite spectrum in the range 215.5–217.5 GHz for the central beam ($5.5'' \times 3.2''$; line 1 of Table 1) toward the source IRAS 16293A (at 0 on the Y-axis) and IRAS 16293B (offset in the Y-axis direction). Transitions of some of the prominent species have been identified.

homogeneously distributed (e.g., less strongly weighted by temperature than the dust continuum emission). This is clearly seen for the CO isotopologues – ^{12}CO at 230.538 GHz and ^{13}CO at 220.398 GHz, as examples – but the "absorption" features seen toward IRAS 16293B for, e.g., N_2D^+ at 231.321 GHz

and CN at 226.875 GHz, also reflect this. In particular, the absence of CN emission in the maps is a clear example of the effects of the interferometer resolving out more extended emission: in pointed JCMT single-dish observations of CN at 226.875 GHz van Dishoeck et al. (1995) found lines with
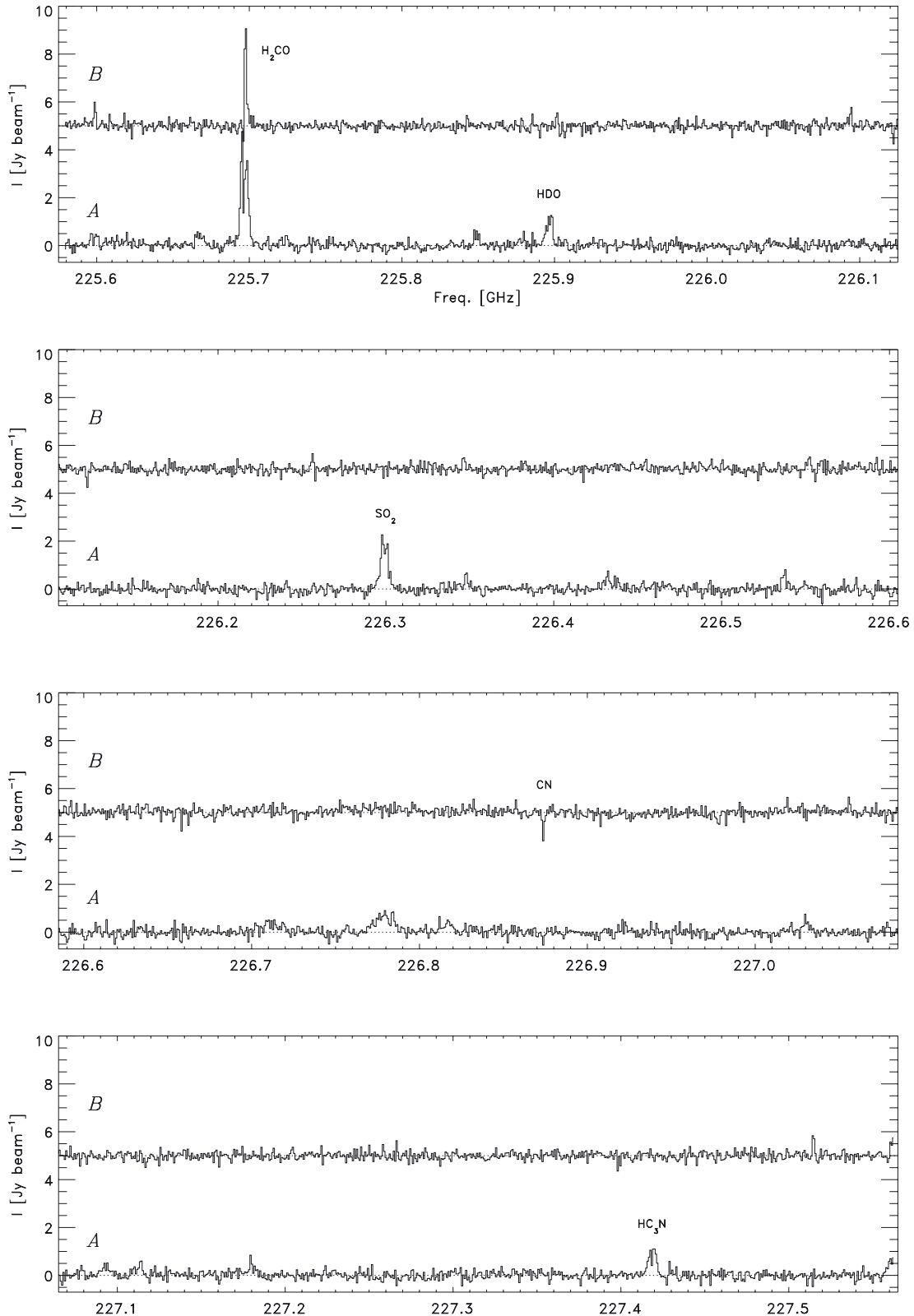
Fig. 3. As in Fig. 2 for the range 225.5–227.5 GHz (beam size 5.5″ × 3.2″; line 1 of Table 1).

intensities of 0.6−0.8 km s^{-1} (10−15 Jy beam^{-1} km s^{-1}), contrasting the absence of CN emission in the SMA maps presented here. As pointed out by van Dishoeck et al., the narrow widths of the CN lines suggests a picture where this species is probing only the outer envelope and ambient core. This would indeed be on spatial scales resolved out by the SMA observations.

The interferometer's spatial filtering makes it difficult to use the interferometric data for quantitative estimates of, e.g., exact column densities or other physical parameters without a careful treatment of the amount of resolved-out emission, for example by combining the interferometric data with short-spacing maps from single-dish telescopes or more detailed models of the
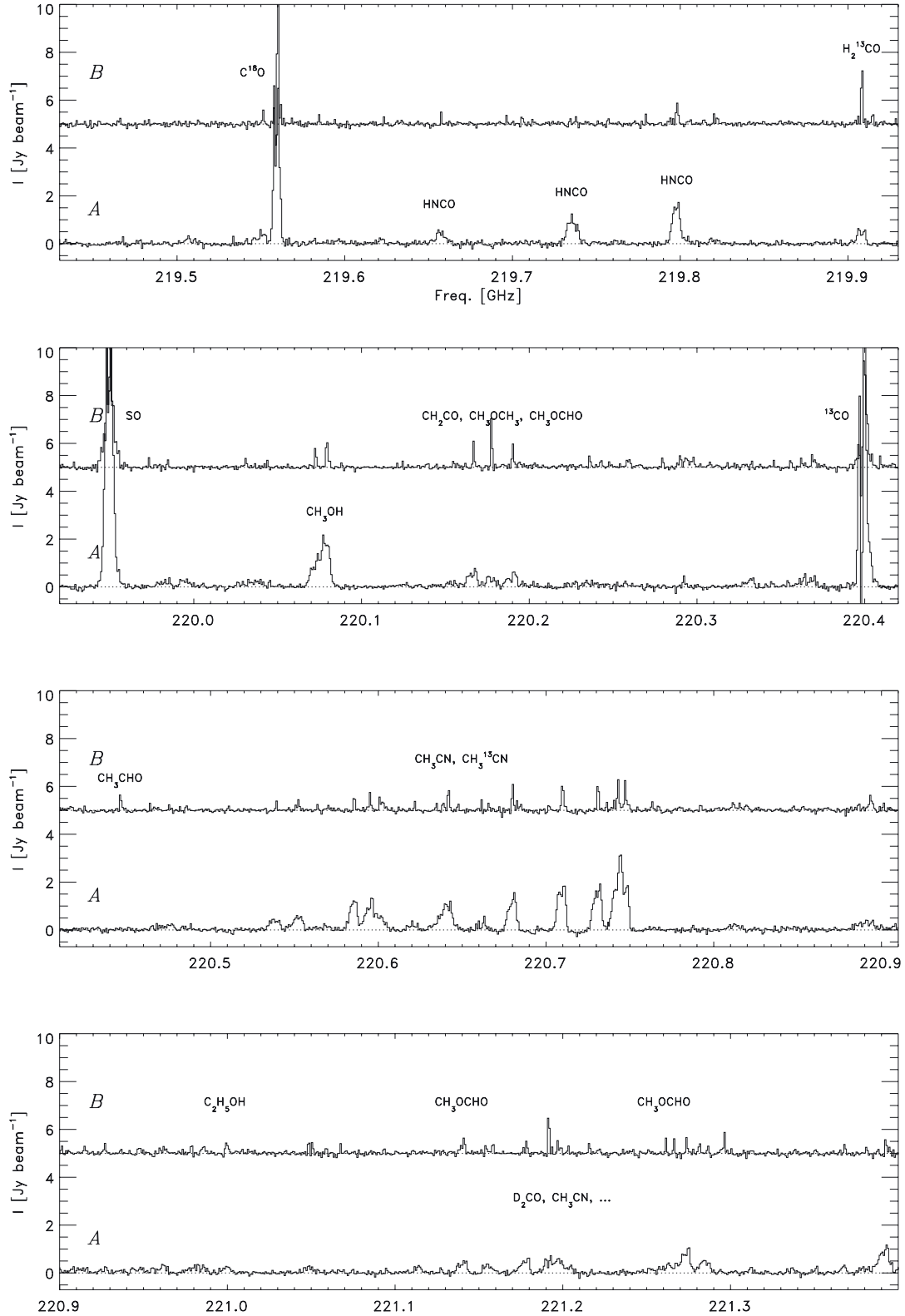
Fig. 4. As in Fig. 2 for the range 219.4–221.4 GHz (beam size 4.0″ × 2.4″; line 2 of Table 1).

source structure (see, e.g., Schöier et al. 2004; and Takakuwa et al. 2007). Still, the interferometric maps reveal the most prominent structures in the surface brightness distributions from the molecular lines – for example where the largest column densities of the different species occur – and therefore allow for a qualitative interpretation of the relations and differences between the imaged molecular species.

Lines present in the spectra toward each of the two continuum peak positions were identified using the CDMS (Müller et al. 2001, 2005) and JPL (Pickett et al. 1998) spectroscopic catalogs: the catalog entries were downloaded for the molecular species expected toward the two protostars, and compared to the observed spectra. Line identifications were made by eye taking into account the excitation energy levels and intrinsic line
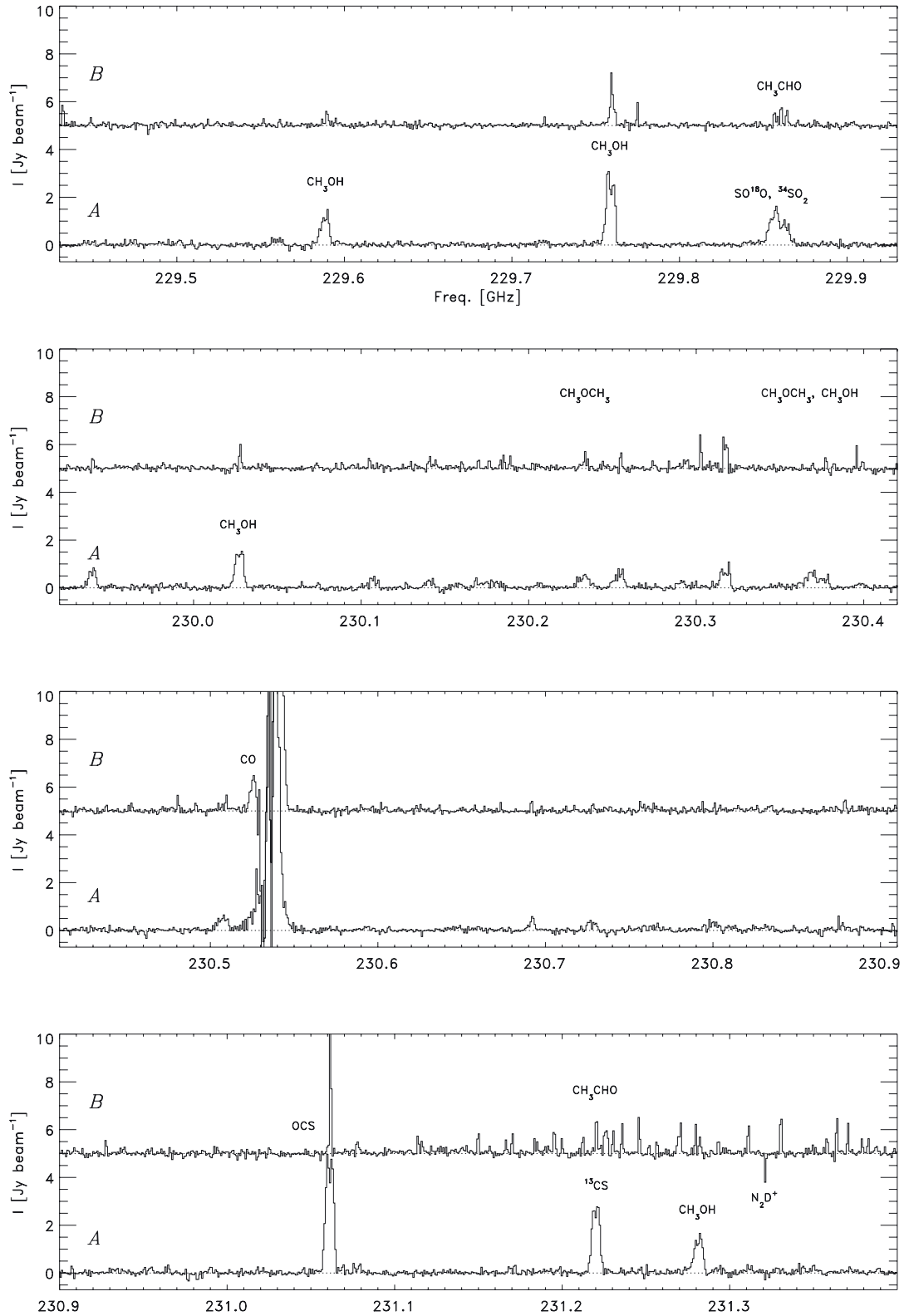
Fig. 5. As in Fig. 2 for the range 229.4–231.4 GHz (beam size 4.0″ × 2.4″; line 2 of Table 1).

strengths when evaluating the detection of a given transition. This process was done iteratively: that is, for detected species lower excited or stronger lines unassigned in the first round were searched for, e.g., looking at possible line blends with stronger lines for other species. Unassigned lines were checked against both catalogs and if a sufficient number of lines of a given molecule was detected, it was included in the search list.

In this manner a total of 515 transitions (996 including tabulated hyperfine components) from 54 molecular species (including isotopologues) were identified. About 10% of the features in the spectra remain unassigned. Table 2 summarizes the detected molecules, the number of lines and the energy ranges for the detected species – while Table A.1 compiles all the identified lines.
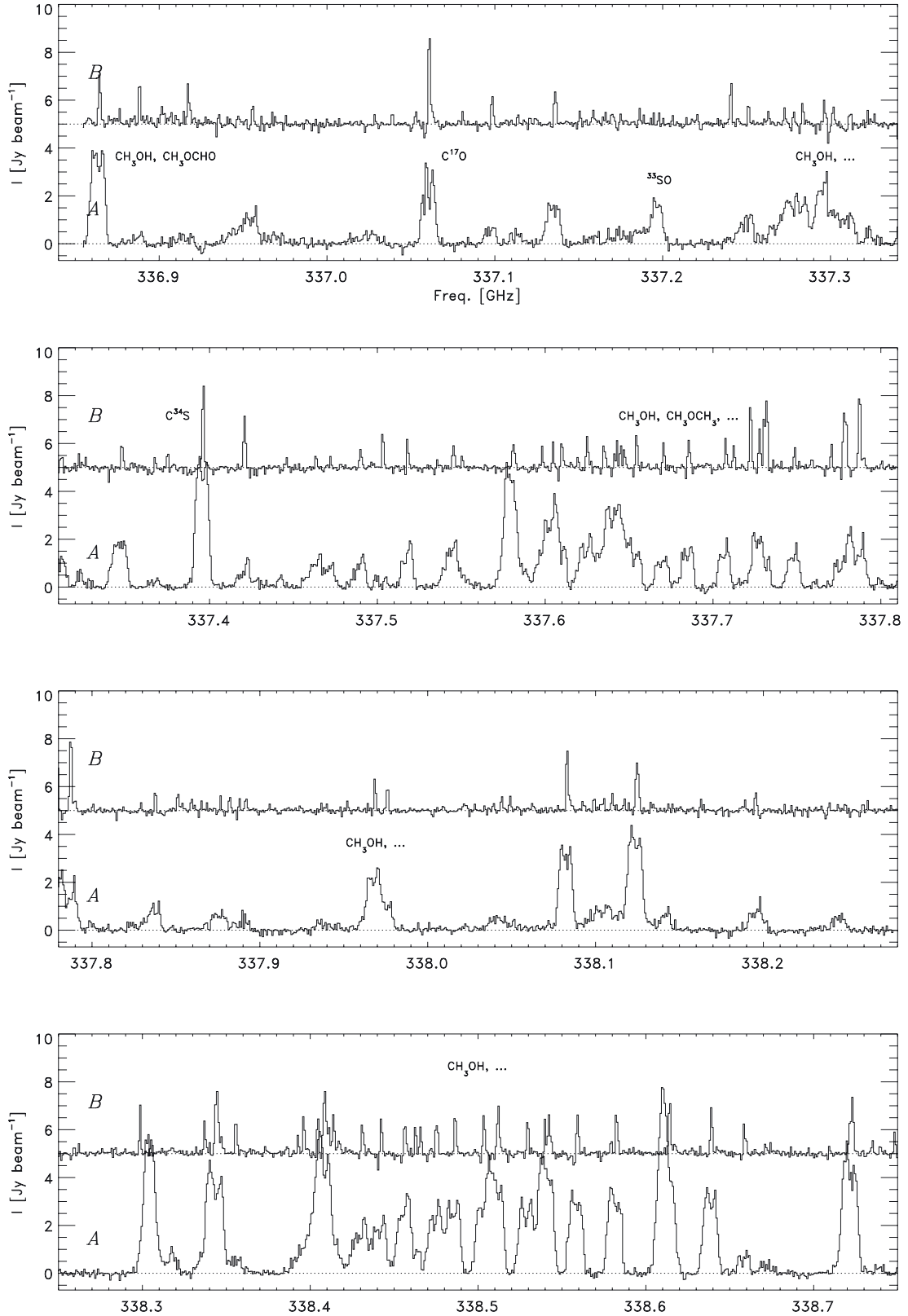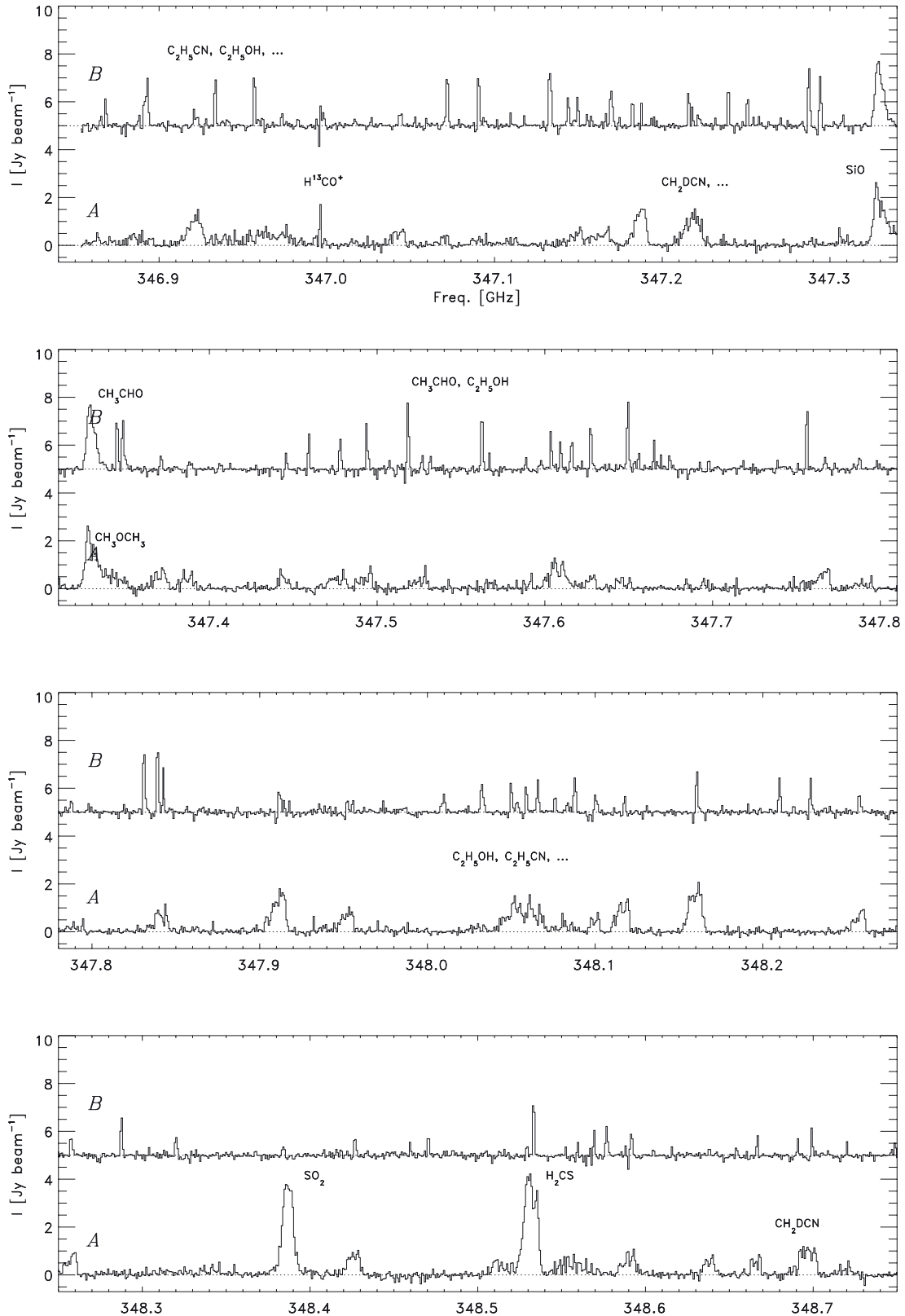
Fig. 6. As in Fig. 2 for the range 336.85–338.85 GHz (beam size 2.5″ × 1.6″; line 3 of Table 1).

Figure 10 shows the cumulative distribution of the upper energy levels, E_u, for the detected molecules – compared to the full catalog entries for the same species over the measured frequency ranges. The figure clearly illustrates the upper limit for the temperatures of the detected species – with approximately 90% of the detected molecular lines having E_u lower than 550 K,

compared to 50% of the catalog entries having E_u lower than this temperature.

For each detected line, the first and second moments (centroid velocity and dispersion) were estimated toward the positions of the two components by numerical integrations of the spectra over velocity intervals of ±5 km s^{-1} around the expected

**Fig. 7.** As in Fig. 2 for the range 346.85–348.85 GHz (beam size 2.5″ × 1.6″; line 3 of Table 1).

systemic velocity of each line at ≈3 km s^{-1}. Figure 11 summarizes the distribution of these velocities. As expected from the above comments and previous findings in literature, the lines toward the IRAS 16293A continuum peak are on average wider and slightly more red-shifted than toward the IRAS 16293B peak (the peaks of the distributions in Fig. 11 shifted toward higher

velocities). However, as illustrated by the figure, the distributions of both centroid velocities and dispersions are broader toward IRAS 16293B than IRAS 16293A. This suggests that the emission toward IRAS 16293B can be divided into a set of lines localized for this source with another set of lines probing the more general environment of both sources in common. It is possible
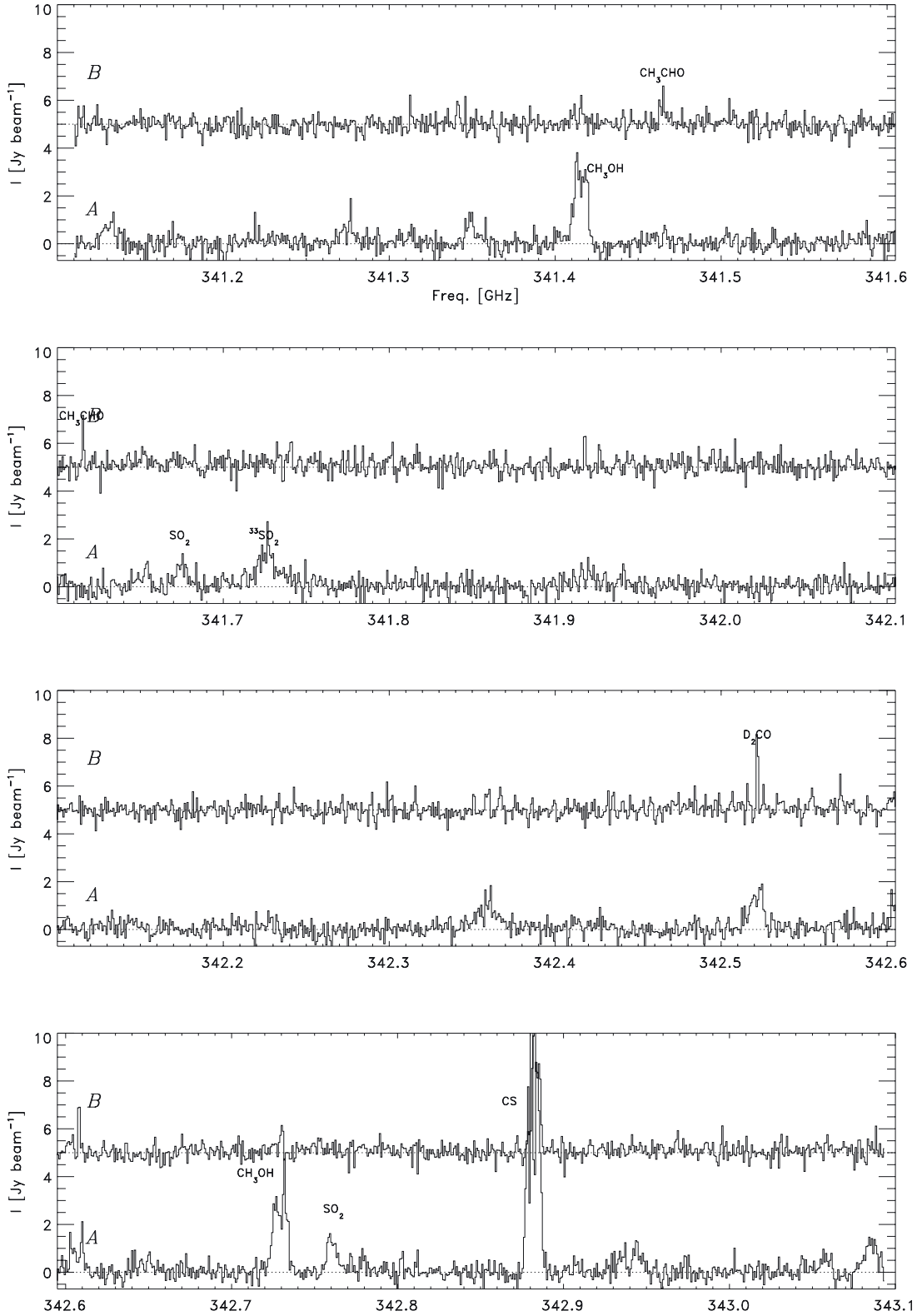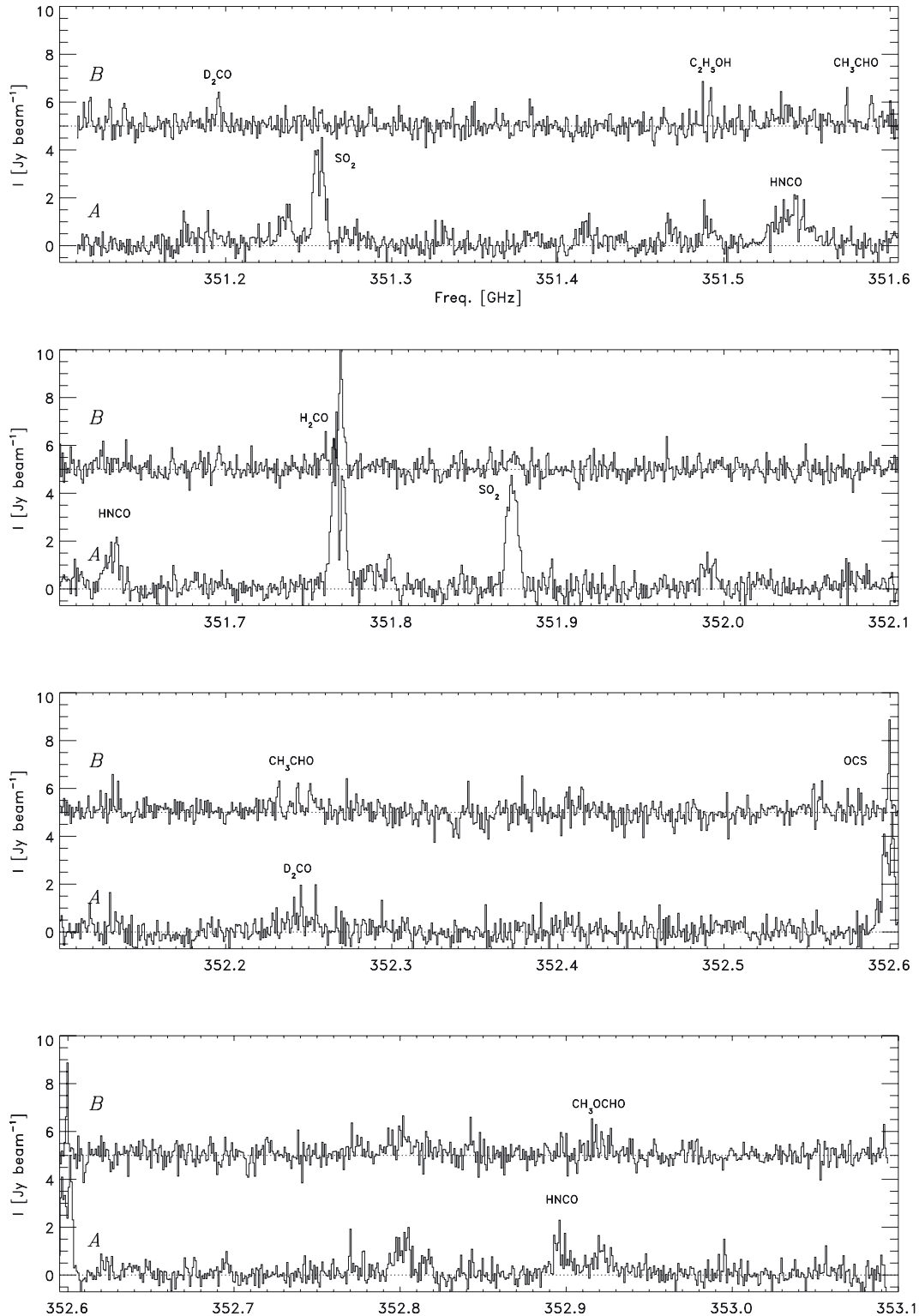
Fig. 8. As in Fig. 2 for the range 341.1–343.3 GHz (beam size 3.5″ × 1.9″; line 4 of Table 1).

that uncertainties in the determined line rest frequencies contribute to some of the scatter in this plot. However, since a large number of the lines are detected in both sources, it is unlikely that these uncertainties introduce the systematic shift and broadening of the lines between the two sources.

For each molecular species the emission from detected, isolated lines were integrated over $V_{sys} \pm \Delta V$ where V_{sys} is the average centroid velocity for the IRAS 16293A component and ΔV the average line width. Compilations of the maps from the inner 24″ × 24″ are shown in Figs. 12−15. In these plots, maps from different transitions for the same molecule have been added together weighted by their noise. For molecules with transitions in multiple frequency bands, data from one band only were used to keep the spatial resolution similar (see Table A.1). For

Fig. 9. As in Fig. 2 for the range 351.1–353.1 GHz (beam size 3.5″ × 1.9″; line 4 of Table 1).

molecules with a large number of detected lines with high S/N spanning a range of energy levels, the integrations were subdivided into integrations over lines in different energy ranges.

4. Results and discussion

In this section we discuss the general features of the detected emission before going into a few more specific topics in detail.

Generally the integrated line emission maps of IRAS 16293-2422 can be divided into groups:

1. Maps with significant extended emission encompassing both sources but without clear peaks or with peaks offset from the continuum sources. Examples: CO, SiO and H_2CO $5_{1,5}-4_{1,4}$.
2. Maps with significant extended emission peaking on one or both continuum sources. Examples: ^{13}CO, $C^{18}O$, $C^{17}O$, CS and isotopologues, SO, H_2CO / $H_2^{13}CO$ $3_{1,2}-2_{1,1}$, $H_2C^{18}O$.

Table 1. Log of observations.

Frequency range [GHz]	Observed date	Beam size[a]	Spectral resolution [km s^{-1}]	Sensitivity [Jy beam^{-1} chan^{-1}]	Projected baselines[b] [kλ]
215.6–217.6 / 225.6–227.6	2004-07-23	5.5″ × 3.2″	0.56	0.24	6–91
219.4–221.4 / 229.4–231.4	2005-02-18	4.0″ × 2.4″	1.1	0.062	7–54
336.8–338.7 / 346.7–348.7	2007-03-22	2.5″ × 1.6″	0.72	0.11	10–141
341.2–343.1 / 351.1–353.1	2005-08-14	3.5″ × 1.9″	0.36	0.60	11–82

Notes. [a] With natural weighting. [b] Range of projected interferometer baselines observed for given dataset measured in kλ.
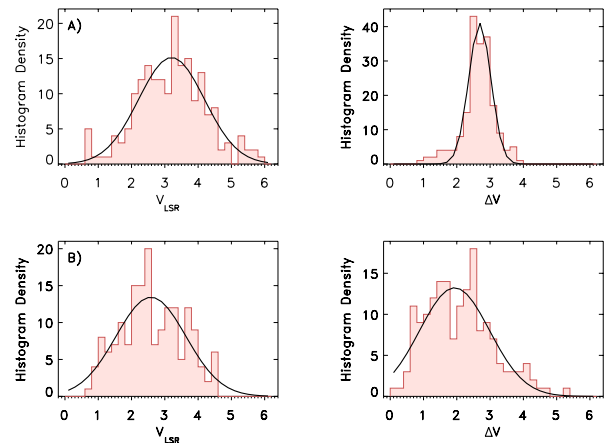
Table 2. Detected molecules.

| Molecules	$n_{\rm lines}$	$E_{\rm u}$ [K]	Molecules	$n_{\rm lines}$	$E_{\rm u}$ [K]	Molecules	$n_{\rm lines}$	$E_{\rm u}$ [K]
CO, HCO$^+$ and N-bearing species
CO	1	16.6	^{13}CO	1	15.9	C^{18}O	1	15.8
C^{17}O	1	32.4	H^{13}CO$^+$	1	41.6	HC$_3$N	1	141.9
H$_2$CN	4	21.1–175.4	CH$_3$CN	20	68.9–1291.5	CH$_3^{13}$CN	8	68.8–646.6
C$_2$H$_5$CN	34	79.1–681.3	HNCO	12	58.0–835.7	HNC^{18}O	1	195.5
O-bearing species
H$_2$CO	3	33.4–174.0	H$_2^{13}$CO	1	32.9	H$_2$C^{18}O	5	97.4–239.6
CH$_3$OH	62	39.8–802.2	^{13}CH$_3$OH	5	87.1–302.5	C$_2$H$_5$OH	37	74.4–1289.1
HCOOH	1	332.7	CH$_2$CO	1	76.5	CH$_3$CHO	101	22.9–864.6
CH$_3$OCH$_3$	26	48.0–952.8	CH$_3$OCHO-A	35	81.4–604.3	CH$_3$OCHO-E	43	56.9–629.8
(CH$_3$)$_2$CO	28	29.9–700.8						
S-bearing species
CS	1	65.8	C^{34}S	1	64.8	^{13}CS	1	33.3
H$_2$S	1	84.0	H$_2$CS	2	102.4–105.2	H$_2$C^{34}S	1	141.8
HCS$^+$	1	73.7	OCS	2	110.9–253.9	O^{13}CS	2	110.5–253.1
SO	1	35.0	^{33}SO	5	25.4–80.5	^{34}SO	2	25.3–34.4
SO$_2$	10	35.9–678.5	^{33}SO$_2$	5	52.4–118.5	^{34}SO$_2$	5	18.7–247.8
SO^{18}O	3	49.0–522.1	SO^{17}O	2	102.8–103.3			
SiO and deuterated species
SiO	2	31.3–75.0	N$_2$D$^+$	1	22.2	DCO$^+$	1	20.7
DCN	1	20.9	HDCS	1	51.5	D$_2$CS	3	105.8–207.5
DCS$^+$	1	36.3	D$_2$CO	6	32.0–285.5	D$_2^{13}$CO	1	57.2
CH$_2$DCN	9	24.1–309.7	HCOOD	2	34.3–386.6	HDO	1	167.6
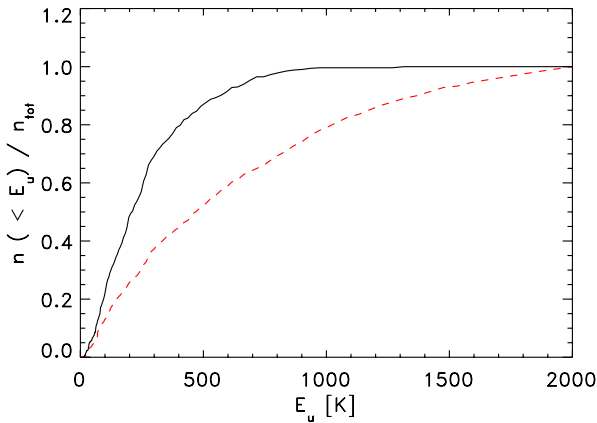
Fig. 10. Cumulative distribution of the upper energy levels for the detected transitions (solid line) and all transitions in the search frequency range for the detected molecules (dashed line).

Fig. 11. Distribution of centroid velocities and widths (dispersions) in the left and right panels, respectively for emission lines detected toward the A source (*upper panels*) and B source (*lower panels*). Gaussian fits to the distributions are over-plotted ($V_{\rm LSR}$ of 3.2 and 2.7 km s^{-1} and ΔV of 2.6 and 1.9 for A and B respectively). The $V_{\rm LSR}$ and ΔV distributions for the two sources are significantly different according to a standard T test for distributions with unequal variances.

3. Maps with localized peaks at the continuum sources, with IRAS 16293A being significantly stronger than IRAS 16293B (the latter in a few cases even absent). Examples: nitrogen- and sulfur-bearing species (including HC$_3$N, CH$_3$CN, HNCO, isotopologues of SO, SO$_2$, OCS among others), most deuterium-bearing species, CH$_3$OH and its ^{13}C isotopologue.

4. Maps with localized peaks at the continuum sources, with the two peaks being approximately similar in strength. Examples: CH$_3$OCH$_3$, CH$_3$OCHO, D$_2$CO.
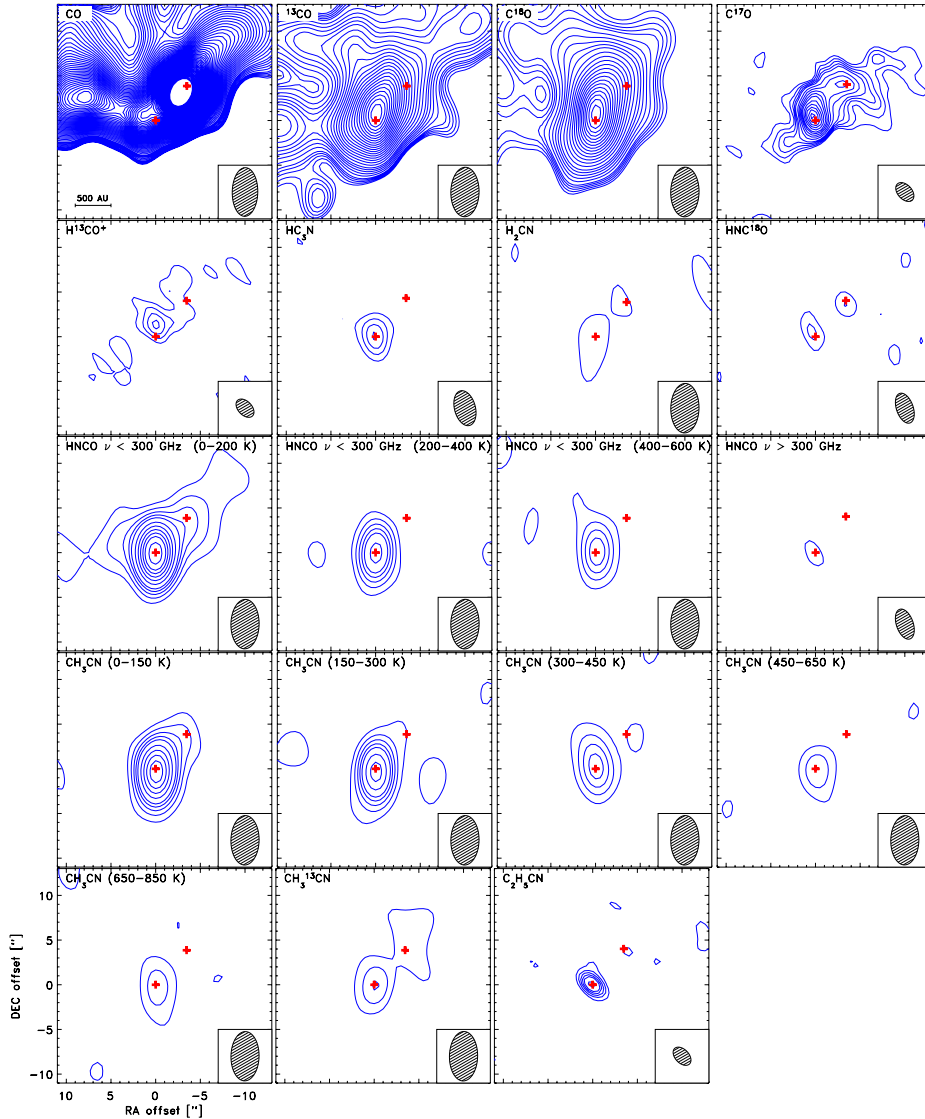
Fig. 12. Emission for CO, HCO$^+$ and the N-bearing organic molecules. For each molecule, except where noted otherwise, the emission has been integrated over all identified lines in one selected frequency band - isolated by at least 10 MHz from other species (see Table A.1 for specific lines). The integration is performed over the width of the "A" component (i.e., from 0 to 6 km s^{-1}) and contours are shown in steps of 3σ to 15σ and in steps of 6σ thereafter, where σ is the rms noise level for the integrated line intensity; the rms per channel is given in Table 1. A scale-bar is shown in the upper left panel. The beam size at the frequency of the selected transitions for the given molecule is shown in the lower right corner of each panel.

5. Maps with localized peaks at the continuum sources, with IRAS 16293B source being stronger than IRAS 16293A. Examples: CH$_3$CHO, CH$_2$CO.

6. Maps with extended faint emission not strongly correlated with the continuum peaks. Examples: N$_2$D$^+$, H^{13}CO$^+$, DCO$^+$.

These maps underline the complicated structure of the protostellar system: the overlap between the emission in, e.g., the extended dense gas tracers suggest that the two sources are embedded in one larger-scale connected envelope, whose column density peaks close to IRAS 16293A. A fainter local maximum in column density is present toward IRAS 16293B, however. The absence of this secondary peak in, e.g., the maps of ^{13}CO and C^{18}O (Fig. 16, upper panels) suggest that these species are becoming optically thick on scales close to the spatial scales probed by the interferometric observations. A particular clear example of that is seen in the emission from $3_{1,2}-2_{1,1}$ transitions

of H$_2$CO and H$_2^{13}$CO: for those two species an inversion is seen with the main H$_2^{12}$CO isotopologue being stronger toward IRAS 16293A while the fainter H$_2^{13}$CO isotopologue is stronger toward IRAS 16293B (Fig. 16, lower panels). The two transitions also appear close to identical in strength in the maps – further indicating a high optical thickness of the main isotopologue and significant resolved-out emission. Optical depth effects and general surface brightness sensitivity may also explain the differences between for example the main isotologue of SO and the fainter species (^{33}SO, ^{34}SO): the latter may also be extended similar to the main isotopologue, but with too low surface brightnesses to be picked up by the SMA observations. A few species show very strongly differentiated emission between the two sources. The sulfur-species (SO$_2$ in particular) are strongly concentrated toward IRAS 16293A while a few of the complex organics (CH$_3$CHO in particular) appear most prominently toward IRAS 16293B. As the lines of the different species are not significantly different in excitation temperatures, these
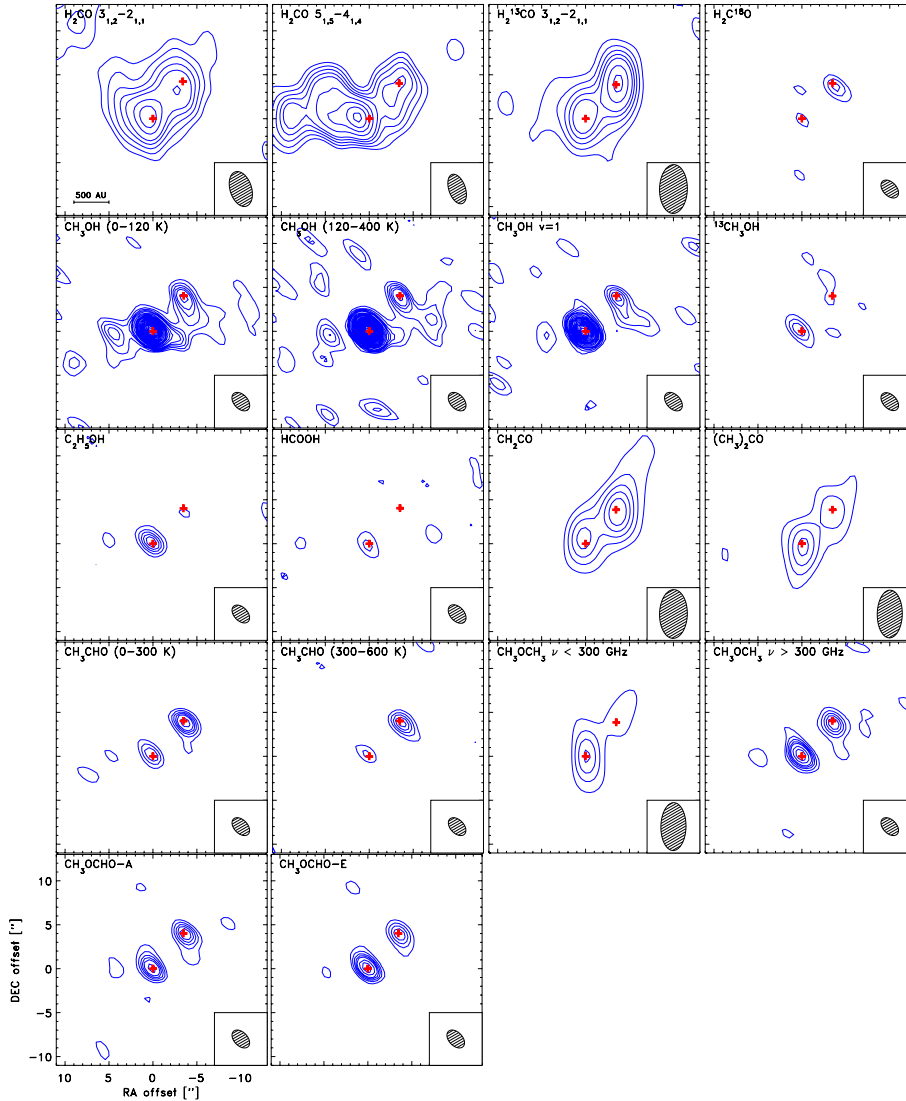
Fig. 13. As in Fig. 12 for the O-bearing organic molecules.

differences in their relative prominences point to different chemical structures of the two components in IRAS 16293-2422 – possibly reflecting differences in their physical evolution.

4.1. Cold envelope chemistry

Although a natural focus in the submillimeter interferometric observations is on the higher excited lines, warmer gas and the small-scale structure close to protostars themselves, the high resolution offered by the interferometric observations provides interesting insights into the chemistry in the colder envelope on large scales. The survey includes a number of species that predominantly are present in the cold $20-30$ K gas and/or very sensitive to changes in chemistry occurring at these temperatures.

One clear example is offered by a comparison between $C^{18}O$, DCO^+ and N_2D^+ (Fig. 17). The emission from these three species are all mainly associated with IRAS 16293A, and all show significant emission extending over $5-10''$ scales. $C^{18}O$ is the species located closest to the continuum peak. DCO^+ is also present there, but shows its maximum offset by $3-4''$. The N_2D^+ transition in contrast does not show any emission at the continuum/$C^{18}O$ peaks, but is offset in the same direction of

DCO^+ with its peak shifted even further. Of course, the "absorption feature" of N_2D^+ toward IRAS 16293B indicates that this species is also present along line of sights toward the central protostars, but simply resolved-out. It is likely that something similar is the case for DCO^+ as well. Still, the maps reveal the differences between the brightest spots in the emission in each of the molecular species, reflecting that their underlying spatial distributions also differ.

Figure 17 shows the temperature from self-consistent dust radiative transfer models of IRAS 16293-2422 (Schöier et al. 2002; Jørgensen et al. 2005a). In those papers, the structure of IRAS 16293-2422 is modeled as a single spherical protostellar dust envelope heated by a central source of luminosity. Using the spectral energy distribution and submillimeter continuum maps to constrain the envelope density structure, the models then calculate the temperature distribution as function of radius self-consistently. For this plot, we locate the envelope at the position of IRAS 16293A and assign half the total luminosity to this source. It is seen that the differentiation between CO, DCO^+ and N_2D^+ is taking place at scales corresponding to the radii of $20-30$ K in the envelope. The comparison to these spherical models is naturally a simplification because of the binarity of the system: the dust and gas in the northern-western part envelope
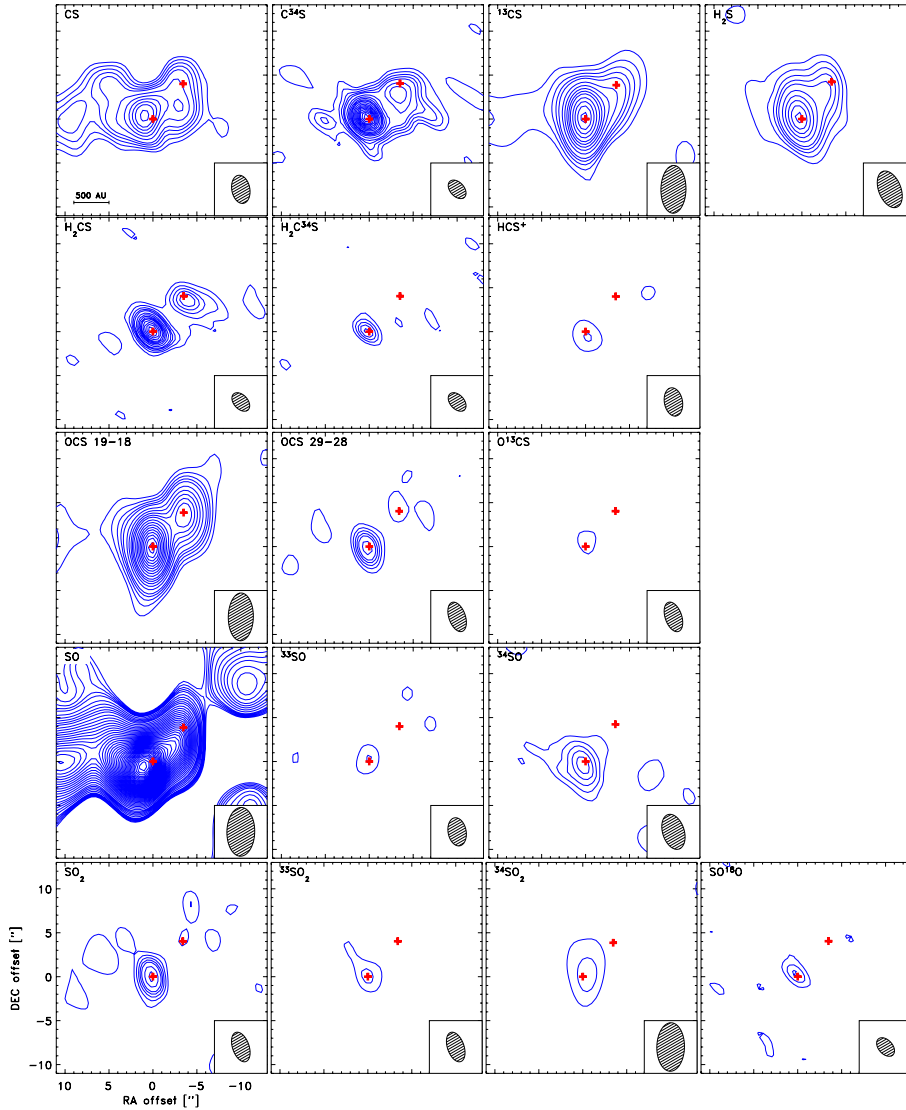
Fig. 14. As in Fig. 12 for the S-bearing molecules.

is likely affected by the presence of IRAS 16293B, as also suggested by the absence of the line emission there.

The differentiation between $C^{18}O$, DCO^+ and N_2D^+ can be understood in the context of the gas-phase chemistry of the cold envelope gas (Fig. 18): CO has been shown to be freezing out significantly at low temperatures in the outer regions of protostellar envelopes, desorbing off the dust grains once the temperature increases to ≈ 30 K (e.g., Jørgensen et al. 2002, 2005b). This gives a primary peak of the $C^{18}O$ emission associated with the compact continuum emission marking the location of the protostar itself as seen in Fig. 17. At larger radii and low temperatures, the freeze-out of CO gives a boost to DCO^+ and N_2D^+: DCO^+ is tied to the CO abundance through the reaction $H_2D^+ + CO \rightarrow DCO^+$. This takes place most efficiently at temperatures lower than 30 K where the amounts of H_2D^+ increases due to the small energy difference in the reaction:

$$H_3^+ + HD \rightarrow H_2D^+ + H_2 \qquad (1)$$

(Roberts & Millar 2000). At temperatures higher than 30 K in contrast, H_2D^+ is rapidly transformed into H_3^+ through reactions with H_2 and then further incorporated into HCO^+ through reactions with CO. This effect is similar for N_2D^+ – except that it is even further enhanced by the fact that any CO present in

the gas will work very efficiently in destroying N_2D^+, thus limiting it even further (N_2H^+ is also enhanced in the colder, CO depleted, gas – because of the lack of its primary destruction agent; see, e.g., Jørgensen et al. 2004). One would therefore expect a sequence in the presence of these three species with CO being present most closely to the center, DCO^+ following this at slightly lower temperatures and N_2D^+ at the lowest temperatures (Fig. 18). This scenario is in qualitative agreement with what is seen in the SMA data with the species peaking at the distances expected from the temperature of the protostellar envelope given its temperature profile in a simple spherical model (Fig. 17).

4.2. The importance of the outflows in IRAS 16293-2422

The outflow activity in IRAS 16293-2422 has been the topic of many discussions in literature – both in terms of the larger scales probed by single-dish observations and on smaller scales trying to identify what outflows are driven by each of the components. CO line emission toward IRAS 16293-2422 show a characteristic quadrupolar structure (Walker et al. 1988), which could reflect its binary nature. Stark et al. (2004) suggested that this quadrupolar morphology could be interpreted as being a superposition of an older outflow in the East-West direction driven by
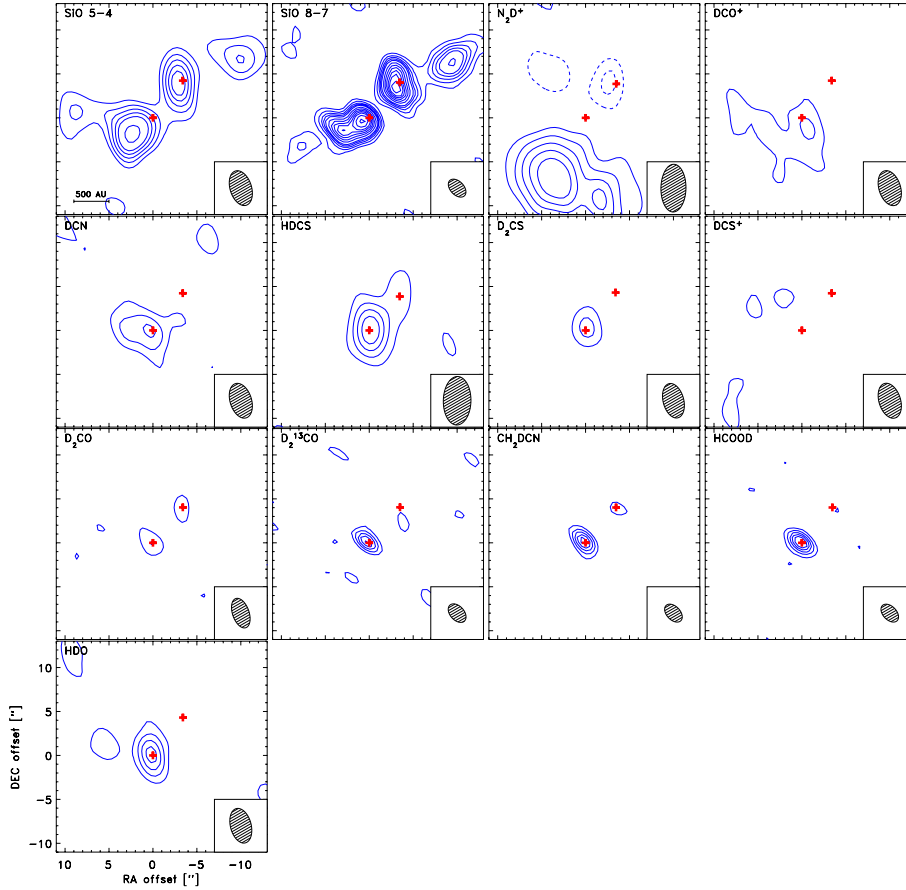
Fig. 15. As in Fig. 12 for SiO and the deuterated molecules. For the N_2D^+ panel the observed "absorption" feature is illustrated by the dashed contours corresponding to negative contour levels.
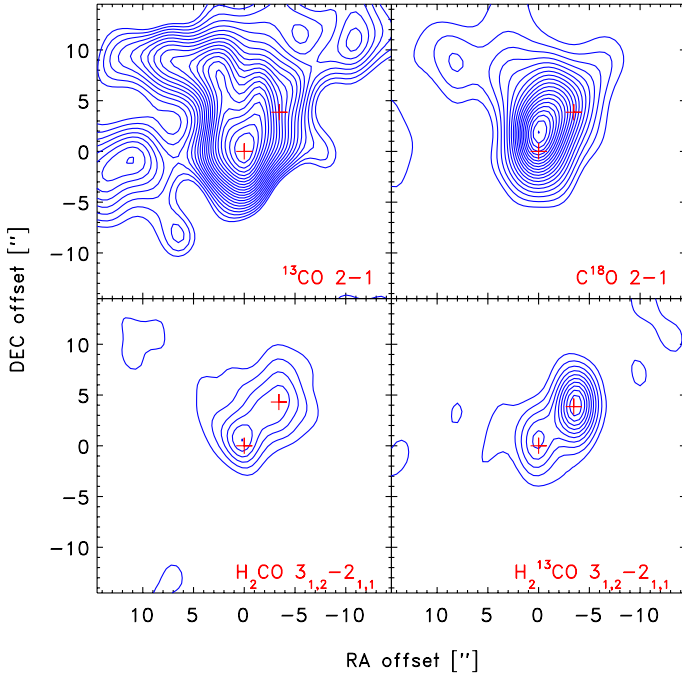

Fig. 16. Comparison between ^{13}CO 2–1 (*upper left*), $C^{18}O$ 2–1 (*upper right*), H_2CO $3_{1,2}-2_{1,1}$ (*lower left*) and $H_2^{13}CO$ $3_{1,2}-2_{1,1}$ (*lower right*). For all species the emission is integrated from 1 to 5 km s^{-1}. The contours are shown in steps of 9 Jy beam^{-1} km s^{-1} for the CO isotopologues and 3 Jy beam^{-1} km s^{-1} for the H_2CO isotopologues.

IRAS 16293B and a younger outflow in the Northeast/Southwest direction driven by IRAS 16293A. This led these authors to suggest that the IRAS 16293B in fact was the older of these two sources – possibly a low luminosity T Tauri star. This view has, however, been challenged by high resolution CO observations showing that the East-West outflow is unambiguously associated with IRAS 16293A (e.g., Yeh et al. 2008). On the smallest scales in the system, it remains an important question if the outflows play a role in regulating the temperature and density structure: through the high angular resolution CO 2–1 and 3–2 maps Yeh et al. (2008) for example showed the existence of two bright spots in their outflow maps offset by about 1″ from the two protostars and toward IRAS16293A in particular, Chandler et al. (2005) showed that excitation transitions of a number of other species were offset likely due to the impact of this outflow (in particular, their Fig. 21).

Besides CO often used tracers of outflow emission are the transitions of SiO (in particular, $J = 2-1$, 5–4 and 8–7) thought to be the result of silicon in atomic form sputtering off dust grains and reacting with OH in the gas-phase producing SiO in the process (e.g., Schilke et al. 1997). The larger scale environment of IRAS 16293-2422 has been mapped in the line of SiO 2–1 with single-dish telescopes (Hirano et al. 2001; Castets et al. 2001) and used for discussions of the relation between the SiO emission and the protostellar outflows.
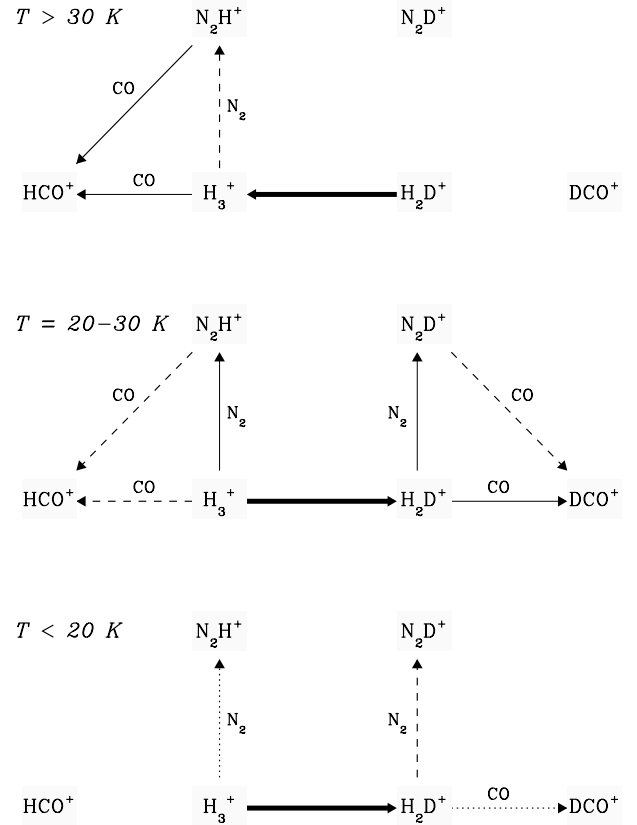
Ceccarelli et al. (2000) discussed multi-transition single-dish observations of the SiO emission at the location of the central protostellar binary and analyzed the emission in the context of models of a spherical collapsing envelope. They demonstrated
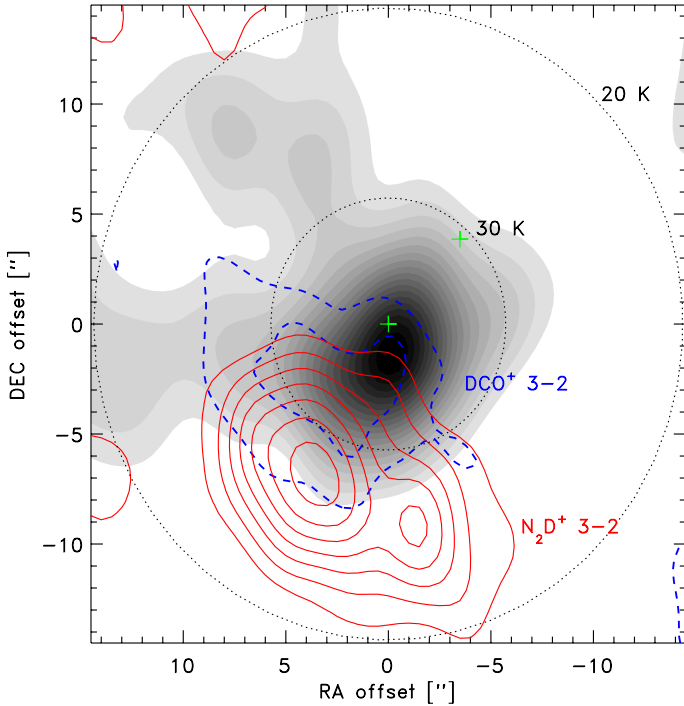
Fig. 17. Comparison between the $C^{18}O$ 2–1 (grey-scale), DCO^+ 3–2 (dashed blue contours) and N_2D^+ 3–2 toward the core. The lines are integrated from velocities of 3–7 km s^{-1} ($C^{18}O$ and N_2D^+) and 4–6 km s^{-1} (DCO^+). The dotted circles indicate the projected radii, where the dust temperature from radiative transfer calculations (Schöier et al. 2002; Jørgensen et al. 2005a) has dropped to 30 K and 20 K, respectively – assuming that the IRAS 16293A component is the sole source of luminosity and that the envelope is centered on this source.

Fig. 18. Schematic chemical network for HCO^+, DCO^+, N_2D^+ and N_2H^+ in different regions of protostellar envelopes: at high temperatures ($T > 30$ K) CO is in the gas-phase and H_3^+ is dominating over H_2D^+ (the reaction in Eq. (1) proceeds to the *left*) enhancing HCO^+ and destroying N_2H^+. At intermediate temperatures ($T = 20{-}30$ K) CO depletion and H_2D^+ production starts to kick-in (the reaction in Eq. (1) proceeds to the *right*), enhancing N_2H^+ (less destruction through CO) and the deuterated species (DCO^+ in particular, through reactions between H_3^+ and CO). At low temperatures CO depletion is very significant and N_2D^+ is enhanced relative to the other species.

that the SiO emission could be explained within this model if the SiO abundance increased from a low ("molecular cloud") value of 4×10^{-12} to a "warm" value of 1.5×10^{-8}. They noted that in this model, the bulk of the observed SiO 5–4 emission arises at a distance less than 150 AU from the central source where the infall velocity is large, about 2.8 km s^{-1} in their model, consistent with the large line width seen in the single-dish observations.

The observations presented here show that this model does not provide an adequate description of the emission morphology of these SiO transitions. In fact, both the $J = 5{-}4$ and 8−7 transitions show emission significantly extended on scales comparable to typical single-dish beams extending over the two protostellar sources with localized peaks close to the two protostars. In IRAS 16293A, the SiO emission peaks slightly east of the central protostar close to the location of the bright CO spot reported by Yeh et al. (2008), whereas the emission toward IRAS 16293B is slightly extended around the position of the central protostar and the CO bright spot associated with that source – but not uniquely associated with either. Generally, very few low-mass protostars show significant SiO line emission (e.g., Jørgensen et al. 2007), so the strong detection toward IRAS 16293-2422 (e.g., Blake et al. 1994) is notable in itself. SiO is thought to be produced by sputtering of silicon of dust grains in shocks, reacting with OH once in the gas-phase. This would suggest that the shock activity is prominent both in the vicinity of IRAS 16293A and IRAS 16293B – despite the absence of a clear CO outflow driven by the latter. It is therefore likely that the outflow driven shock is affecting the physics and chemistry of the gas in the immediate vicinity of IRAS 16293B. Higher resolution observations of the kinematics of the gas at this position are needed to

clarify the importance of these shocks compared to the radiation by the embedded protostar.

4.2.1. HDO emission

Clearly the outflows in the IRAS 16293-2422 have an impact on the emission on large scales. Some care therefore needs to be taken in interpreting (unresolved) single-dish observations of the system – in particular, for discussing molecules tracing small-scale structures. A few examples, of species probing gas affected by the outflow emission are CS, CH_3OH and HDO. The two former species are known to be tracers of dense envelope gas affected by outflow emission in protostellar systems (e.g., Jørgensen et al. 2005c), but the latter is particular noteworthy: the SMA data encompass the HDO $3_{12}{-}2_{21}$ transition at 225.896 GHz, a relatively high excitation transition of HDO, which potentially could reveal the presence and distribution of (deuterated) water in this low-mass protostar.

Figure 20 compares the integrated HDO emission to that of SiO 5–4. The maps show two major peaks of the HDO line. One is associated with I16293A and one offset at about (5″, 0″). A third peak is seen at even larger distances – but channel maps (Fig. 21) suggests that this is an extension of the secondary peak. Figure 21 shows the channel maps of the HDO transition
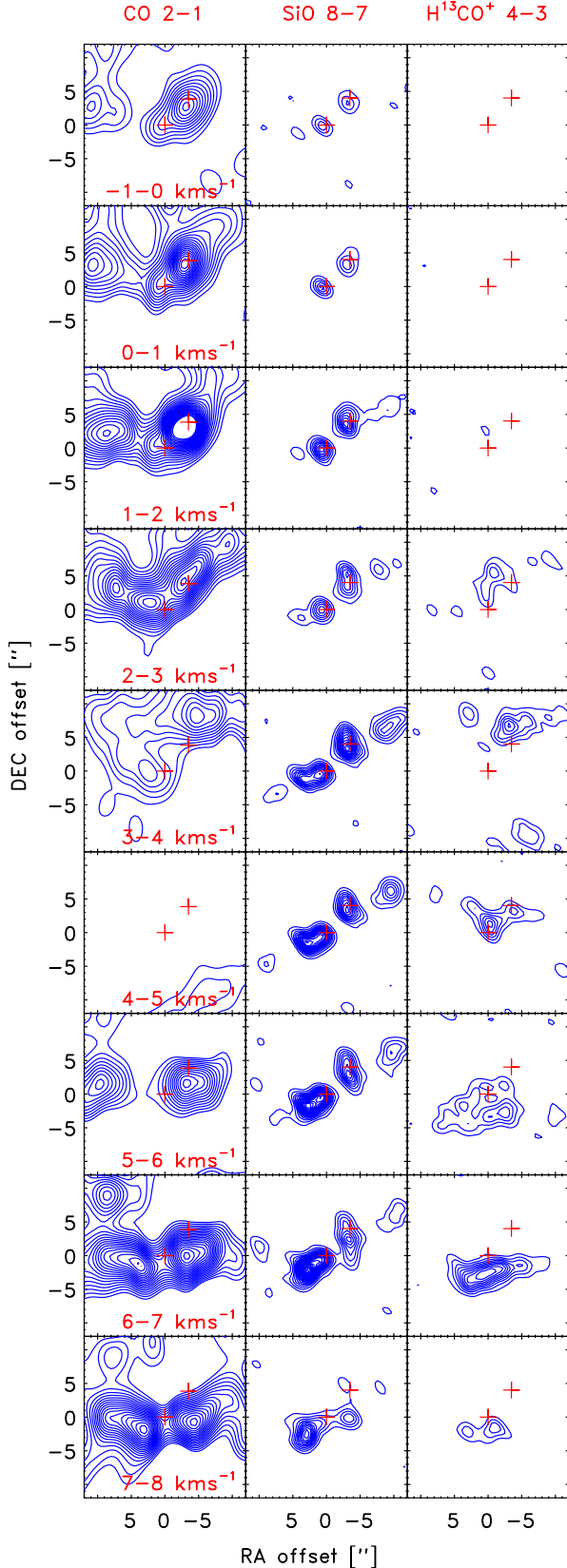
Fig. 19. Channel maps for CO 2–1 (*left column*), SiO 8–7 (*middle column*) and H^{13}CO$^+$ 4–3 (*right column*). Contours are given in steps of 20σ for CO 2–1 and 3σ for SiO 8–7 and H^{13}CO$^+$ 4–3.

and Fig. 22 spectra toward these three positions. The emission at continuum peak is seen most prominently at the systemic
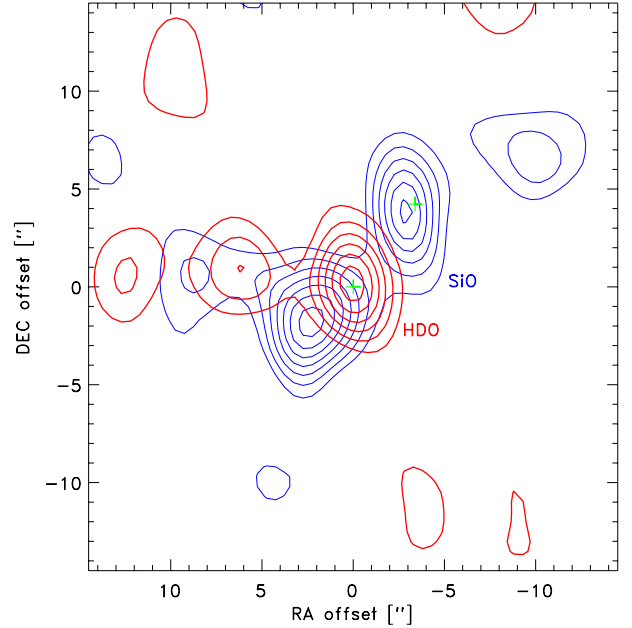
Fig. 20. HDO (225.9 GHz; red) and SiO (217.1 GHz; blue) maps compared. Both datasets were integrated over the velocity range from −1 to 6 km s^{-1}. The contours are given in steps of 3σ.
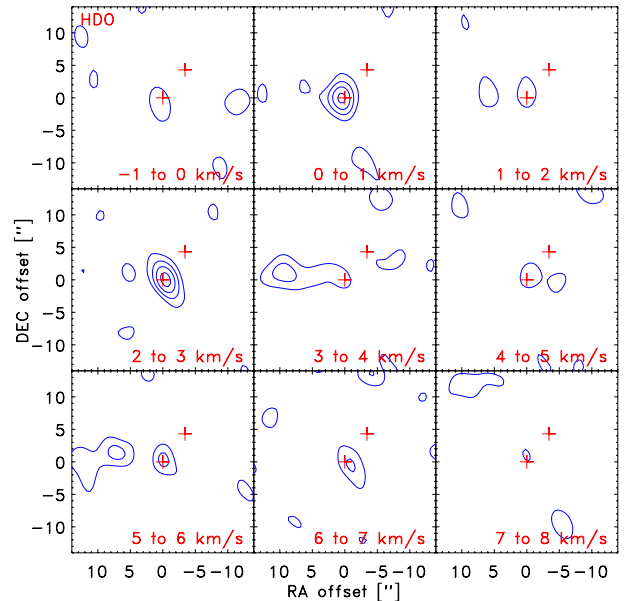

Fig. 21. Channel maps (averaged over 2 channels/1.1 km s^{-1}) of HDO (velocities given in upper right corner of each panel). The HDO data have had a taper of 3″ applied.

velocity, V_{LSR}, of the majority of the lines in the data at about 4 km s^{-1}. The second peak east of the IRAS 16293A continuum position is redshifted relative to this but still extending around the systemic velocity. The morphology of the HDO emission appear related although not directly correlated to that of SiO: generally the HDO emission peaks appear in "valleys" of the red-shifted lobe of the SiO outflow emission (Fig. 20).

5. Summary

This paper has presented a large SMA imaging survey of the line emission from molecular species toward the deeply embedded, Class 0, protostellar binary IRAS 16293-2422 down
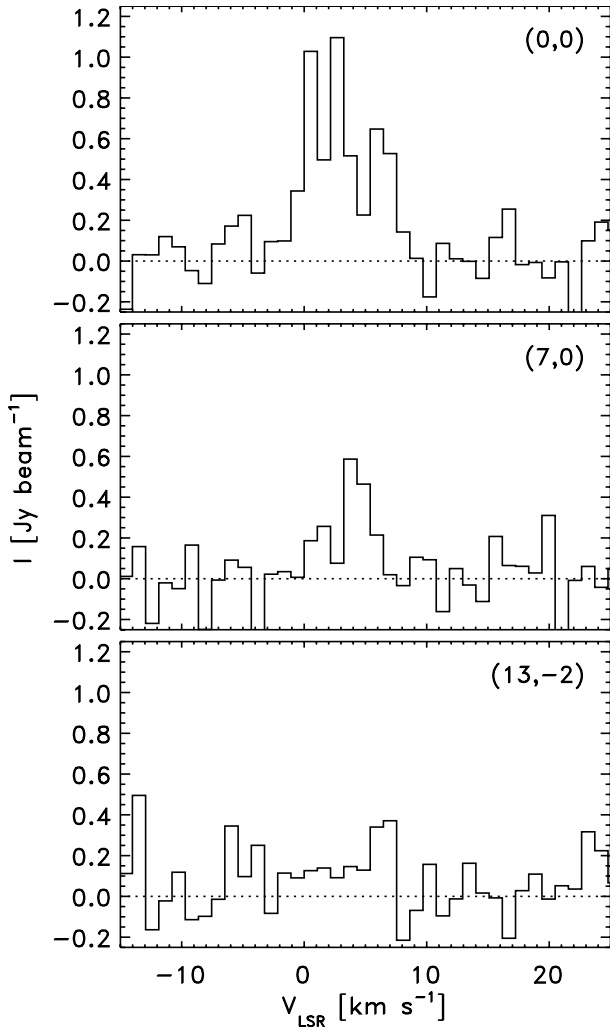
Fig. 22. Representative spectra of HDO in the central beams from maps with a 3″ taper applied (see also Fig. 21) toward the continuum peak of IRAS 16293A, the secondary peak and a position further offset toward the east where the emission is extended the offsets relative to the position of IRAS 16293A in arcseconds given in the upper right corner of each panel.

to 1.5−3″ (190−380 AU) resolution scales. We have identified the molecular line emission toward each of the two components in the protostellar binary and discuss some general features of the emission.

- 515 transitions of 54 species (including isotopologues) are identified. 90% of the identified transitions have upper level energies lower than 550 K. A richness of both non-organic and organic molecules (of varying complexity) are seen toward both binary components.
- Significantly narrower lines are observed toward IRAS 16293B than IRAS 16293A in the system (1.9 km s^{-1} for IRAS 16293B vs. 2.6 km s^{-1} for IRAS 16293A) and the lines toward IRAS 16293B are found to be blue-shifted by about 0.5 km s^{-1} compared to IRAS 16293A as well.
- The molecular species show significantly different strengths relatively at the two components. IRAS 16293A in general has the stronger emission and shows many nitrogen and sulfur-bearing species weak or absent toward IRAS 16293B. The latter in contrast harbors a number of stronger transitions from oxygen-bearing complex organics – in particular, CH$_3$CHO, which is very faint toward IRAS 16293A (see also

Bisschop et al. 2008). There is no evidence for significantly different excitation conditions in the two sources, however.

- Outflowing motions are clearly witnessed by the maps of CO (see also Yeh et al. 2008) and SiO. The latter shows extended emission toward IRAS 16293A but notably very compact emission near IRAS 16293B suggesting the presence of shocks in the immediate vicinity of this source.
- A few specific examples are discussed. More extended emission from N$_2$D$^+$, DCO$^+$ and CO shows differences that can be attributed to cold gas-phase chemistry on large scales in the outer parts of the protostellar core. The emission from deuterated water (HDO) is only present toward IRAS 16293A with evidence for some water coming off dust grains in regions impacted by the protostellar outflow traced by SiO.

The data presented in this paper illustrate the potential of (and need for) high angular resolution imaging when discussing the physics and chemistry of nearby embedded low-mass protostars based on submillimeter wavelength observations – and caution against over-interpretations based on lower resolution data in complex systems such as IRAS 16293-2422. On the other hand, the wealth of information in these and similar studies provide many independent, strong constraints and could be used to shed light on some of the unanswered questions concerning the physical and chemical structure and evolution of low-mass protostars. Once the Atacama Large Millimeter Array (ALMA) is fully operational with its large spectral bandwidth (up to 8 GHz in each of two sidebands) and collecting area, similar types of observations will be routinely done and thus provide a significant boost to studies of the molecular astrophysics in star-forming regions. The data presented in this paper will guide higher sensitivity and resolution observations with ALMA, but also contain a wealth of information in their own right. We therefore welcome everyone to make use of these data and make them publicly available.

References

Bisschop, S. E., Jørgensen, J. K., Bourke, T. L., Bottinelli, S., & van Dishoeck, E. F. 2008, A&A, 488, 959

Blake, G. A., van Dishoek, E. F., Jansen, D. J., Groesbeck, T. D., & Mundy, L. G. 1994, ApJ, 428, 680

Bottinelli, S., Ceccarelli, C., Neri, R., et al. 2004, ApJ, 617, L69

Castets, A., Ceccarelli, C., Loinard, L., Caux, E., & Lefloch, B. 2001, A&A, 375, 40

Caux, E., Kahane, C., Castets, A., et al. 2011, A&A, 532, A23

Cazaux, S., Tielens, A. G. G. M., Ceccarelli, C., et al. 2003, ApJ, 593, L51

Ceccarelli, C., Caux, E., White, G. J., et al. 1998, A&A, 331, 372

Ceccarelli, C., Castets, A., Caux, E., et al. 2000, A&A, 355, 1129

Ceccarelli, C., Caselli, P., Herbst, E., Tielens, A. G. G. M., & Caux, E. 2007, in Protostars and Planets V, ed. B. Reipurth, D. Jewitt, & K. Keil, 47

Chandler, C. J., Brogan, C. L., Shirley, Y. L., & Loinard, L. 2005, ApJ, 632, 371

Herbst, E., & van Dishoeck, E. F. 2009, ARA&A, 47, 427

Hirano, N., Mikami, H., Umemoto, T., Yamamoto, S., & Taniguchi, Y. 2001, ApJ, 547, 899

Ho, P. T. P., Moran, J. M., & Lo, K. Y. 2004, ApJ, 616, L1

Jørgensen, J. K., Schöier, F. L., & van Dishoeck, E. F. 2002, A&A, 389, 908
Jørgensen, J. K., Schöier, F. L., & van Dishoeck, E. F. 2004, A&A, 416, 603
Jørgensen, J. K., Lahuis, F., Schöier, F. L., et al. 2005a, ApJ, 631, L77
Jørgensen, J. K., Schöier, F. L., & van Dishoeck, E. F. 2005b, A&A, 435, 177
Jørgensen, J. K., Schöier, F. L., & van Dishoeck, E. F. 2005c, A&A, 437, 501
Jørgensen, J. K., Bourke, T. L., Myers, P. C., et al. 2007, ApJ, 659, 479
Kuan, Y., Huang, H., Charnley, S. B., et al. 2004, ApJ, 616, L27
Müller, H. S. P., Thorwirth, S., Roth, D. A., & Winnewisser, G. 2001, A&A, 370, L49
Müller, H. S. P., Schlöder, F., Stutzki, J., & Winnewisser, G. 2005, J. Mol. Struct., 742, 215
Mundy, L. G., Wootten, A., Wilking, B. A., Blake, G. A., & Sargent, A. I. 1992, ApJ, 385, 306
Pech, G., Loinard, L., Chandler, C. J., et al. 2010, ApJ, 712, 1403
Pickett, H. M., Poynter, I. R. L., Cohen, E. A., et al. 1998, J. Quant. Spec. Radiat. Transf., 60, 883
Qi, C. 2008, The MIR Cookbook, The Submillimeter Array/Harvard-Smithsonian Center for Astrophysics, http://cfa-www.harvard.edu/~cqi/mircook.html

Remijan, A. J., & Hollis, J. M. 2006, ApJ, 640, 842
Roberts, H., & Millar, T. J. 2000, A&A, 361, 388
Sault, R. J., Teuben, P. J., & Wright, M. C. H. 1995, in Astronomical Data Analysis Software and Systems IV, ed. R. A. Shaw, H. E. Payne, & J. J. E. Hayes, PASP Conf. Ser., 77, 433
Schilke, P., Walmsley, C. M., Pineau des Forets, G., & Flower, D. R. 1997, A&A, 321, 293
Schöier, F. L., Jørgensen, J. K., van Dishoeck, E. F., & Blake, G. A. 2002, A&A, 390, 1001
Schöier, F. L., Jørgensen, J. K., van Dishoeck, E. F., & Blake, G. A. 2004, A&A, 418, 185
Stark, R., Sandell, G., Beck, S. C., et al. 2004, ApJ, 608, 341
Takakuwa, S., Ohashi, N., Bourke, T. L., et al. 2007, ApJ, 662, 431
van Dishoeck, E. F., & Blake, G. A. 1998, ARA&A, 36, 317
van Dishoeck, E. F., Blake, G. A., Jansen, D. J., & Groesbeck, T. D. 1995, ApJ, 447, 760
Walker, C. K., Lada, C. J., Young, E. T., & Margulis, M. 1988, ApJ, 332, 335
Wootten, A. 1989, ApJ, 337, 858
Yeh, S. C. C., Hirano, N., Bourke, T. L., et al. 2008, ApJ, 675, 454

Appendix A: Compilation of all identified emission lines

Table A.1. Compilation of all identified emission lines.

Frequency	Molecule	Transition	$\log(\mu^2 S)^a$	E_u [K]^b	Flag^c	Plot^d
215.8399200	^{34}SO	$5_6 - 4_5$	1.15	34.38	A	+
216.1097290	CH$_3$OCHO-E	$19_{2,18} - 18_{2,17}$	1.69	109.34	B	-
216.1125822	DCO$^+$	$3 - 2$	1.66	20.74	A	+
216.1154858	CH$_3$OCHO-A	$19_{2,18} - 18_{2,17}$	1.69	109.32	B	-
216.2065780	DCS$^+$	$6 - 5$	1.36	36.32	A	+
216.2947260	CH$_3$CHO	$11_{1,10,5} - 10_{1,9,5}$	2.14	269.62	B	-
216.5686510	H$_2$CO	$9_{1,8} - 9_{1,9}$	0.54	173.99	1	+
216.5819360	CH$_3$CHO	$11_{1,10,2} - 10_{1,9,2}$	2.14	64.87	B	-
216.6302210	CH$_3$CHO	$11_{1,10,0} - 10_{1,9,0}$	2.14	64.81	B	-
216.6433035	SO$_2$	$22_{2,20} - 22_{1,21}$	1.55	248.44	A	-
216.7104365	H$_2$S	$2_{2,0} - 2_{1,1}$	0.31	83.98	1	+
216.8388463	CH$_3$OCHO-A	$18_{2,16} - 17_{2,15}$	1.66	105.67	1	-
216.9456000	CH$_3$OH	$5_{1,4} - 4_{2,2}(A+)$	0.05	55.87	1	-
216.9655183	CH$_3$OCHO-E	$20_{2,19} - 19_{1,19}$	2.09*	90.67	1	-|
216.9666519	CH$_3$OCHO-A	$20_{0,20} - 19_{1,19}$	2.09*	90.65	1	-|
217.1049800	SiO	$5 - 4$	1.68	31.26	1	+
217.2370538	CH$_3$OCH$_3$	$34_{7,28,2} - 33_{8,25,2}$	2.07*	590.64	1	-
217.2385378	DCN	$3 - 2$	1.91	20.85	1	+|
217.2992020	CH$_3$OH	$6_{1,5} - 7_{2,6}, v = 1(-E)$	0.67	373.92	1	-
219.4681426	CH$_3$OCH$_3$	$28_{5,24,2} - 27_{6,21,2}$	2.00*	384.79	1	+
219.5055900	C$_2$H$_5$CN	$24_{2,22} - 23_{2,21}$	2.55	135.62	A	-
219.5063307	H$_2$CN	$9_{1,8,19,8} - 9_{1,9,19,8}$	-4.92	175.40	A	-|
219.5470997	HNCO	$10_{4,6,9} - 9_{4,5,9}$	2.11*	729.27	A	-
219.5529227	HN^{13}CO	$10_{4,6,9} - 9_{4,5,9}$	2.11*	727.58	1	-
219.5603541	C^{18}O	$2 - 1$	-1.61	15.81	1	+
219.6218327	C$_2$H$_5$CN	$54_{6,48} - 53_{7,47}$	1.13	681.29	1	-
219.6238599	H$_2$CN	$3_{0,3,2,5} - 2_{0,2,0,5}$	-4.86	21.12	A	-
219.6567105	HNCO	$10_{3,8,9} - 9_{3,7,9}$	2.15*	426.37	1	+
219.7056522	C$_2$H$_5$OH	$43_{2,42,0} - 42_{3,40,1}$	1.06	822.87	B	-
219.7355213	HNCO	$10_{2,9,9} - 9_{2,8,9}$	2.17*	210.01	1	+
219.7983198	HNCO	$10_{0,10,9} - 9_{0,9,9}$	1.89*	36.92	1	+
219.8196052	(CH$_3$)$_2$CO	$21_{12,10,0} - 20_{13,7,0}$	1.35	183.25	1	+
219.9085250	H$_2$^{13}CO	$3_{1,2} - 2_{1,1}$	1.64	32.94	1	+
219.9494420	SO	$5_6 - 4_5$	1.15	34.98	1	+
219.9839950	CH$_3$OH	$25_{3,22} - 24_{4,20}(A+)$	0.92	802.16	1	-
219.9939390	CH$_3$OH	$23_{5,19} - 22_{6,17}(A+)$	0.82	775.88	1	-
219.9969407	(CH$_3$)$_2$CO	$32_{7,25,0} - 32_{7,26,1}$	3.33*	317.44	A	-
220.0784900	CH$_3$OH	$8_{0,8} - 7_{1,6}(A+)$	0.54	96.61	1	-
220.1651979	(CH$_3$)$_2$CO	$19_{16,4,0} - 19_{13,6,1}$	0.34	168.30	A	-|
220.1668155	CH$_3$OCHO-E	$17_{2,15} - 16_{4,12}$	1.63	103.15	1	-
220.1687526	(CH$_3$)$_2$CO	$32_{7,25,0} - 32_{7,26,0}$	3.03*	317.43	A	-|
220.1781956	CH$_2$CO	$11_{1,11} - 10_{1,10}$	1.82	76.48	1	+
220.1843344	CH$_3$OCH$_3$	$32_{15,17,0} - 33_{14,20,0}$	1.98*	774.86	1	-
220.1902269	CH$_3$OCHO-A	$17_{4,13} - 16_{4,12}$	1.63	103.14	1	-
220.2350419	CH$_3$CN	$12_{11,0,12} - 11_{11,0,11}$	2.25*	910.24	B	+
220.2961130	CH$_3$^{13}CN	$12_{9,12} - 11_{9,11}$	2.98*	625.50	B	+
220.3461944	H$_2$CN	$9_{1,8,5,10} - 9_{1,9,5,10}$	-4.82	175.37	A	+
220.3597073	(CH$_3$)$_2$CO	$22_{1,22,1} - 21_{1,21,1}$	3.95*	102.83	1	+
220.3640282	(CH$_3$)$_2$CO	$22_{1,22,0} - 21_{1,21,0}$	3.95*	102.74	1	-
220.3676372	(CH$_3$)$_2$CO	$11_{11,1,1} - 10_{10,1,2}$	2.54	62.89	1	-|
220.3677269	CH$_3$^{13}CN	$12_{8,12} - 11_{8,11}$	2.79*	504.37	1	-|
220.3986842	^{13}CO	$2 - 1$	-1.31	15.87	1	+
220.4013740	CH$_3$OH	$10_{5,5} - 11_{4,8}(A-)$	0.28	251.64	1	-
220.4464450	CH$_3$CHO	$13_{3,10,2} - 13_{2,11,2}$	1.15	104.67	B	-
220.4667117	H$_2$CN	$3_{2,2,23,1} - 2_{2,1,21,1}$	-4.57	68.66	A	+
220.4758142	CH$_3$CN	$12_{8,0,12} - 11_{8,0,11}$	2.79*	504.40	1	+
220.4858600	CH$_3$^{13}CN	$12_{6,12} - 11_{6,11}$	3.22*	304.69	1	+
220.5393300	CH$_3$CN	$12_{7,0,12} - 11_{7,0,11}$	2.86*	397.45	1	+
220.5511144	(CH$_3$)$_2$CO	$12_{8,5,0} - 11_{7,5,1}$	0.21	63.84	1	+
220.5703792	CH$_3$^{13}CN	$12_{4,12} - 11_{4,11}$	2.99*	161.94	1	+
220.5851975	HNCO	$10_{1,9,9} - 9_{1,8,9}$	1.88*	80.33	1	+
220.5944295	CH$_3$CN	$12_{6,0,12} - 11_{6,0,12}$	3.22*	304.72	1	-

Table A.1. continued.

Frequency	Molecule	Transition	$\log(\mu^2 S)^a$	E_u [K]^b	Flag^c	Plot^d
220.5999883	CH$_3$^{13}CN	$12_{3,12} - 11_{3,11}$	3.32*	111.95	1	-
220.6019270	C$_2$H$_5$OH	$13_{1,13,2} - 12_{0,12,2}$	1.18	74.44	1	-
220.6211464	CH$_3$^{13}CN	$12_{2,12} - 11_{2,11}$	3.03*	76.23	1	+
220.6338478	CH$_3$^{13}CN	$12_{1,12} - 11_{1,11}$	2.88*	54.80	1	-
220.6380781	CH$_3$^{13}CN	$12_{0,11} - 11_{0,10}$	3.04*	47.65	1	-
220.6411217	CH$_3$CN	$12_{5,0,12} - 11_{5,0,11}$	2.96*	226.22	1	-
220.6609152	C$_2$H$_5$CN	$25_{2,24} - 24_{2,23}$	2.57	143.02	B	-
220.6648874	(CH$_3$)$_2$CO	$11_{11,1,0} - 10_{10,1,1}$	3.14	62.92	1	-
220.6793199	CH$_3$CN	$12_{4,0,12} - 11_{4,0,12}$	2.99*	161.96	1	+
220.7090798	CH$_3$CN	$12_{3,0,12} - 11_{3,0,12}$	3.32*	111.97	1	-
220.7104700	CH$_3$OCHO-E	$24_{2,22} - 24_{1,24}$	0.34*	147.64	1	-
220.7302701	CH$_3$CN	$12_{2,0,12} - 11_{2,0,12}$	3.03*	76.25	1	+
220.7429903	CH$_3$CN	$12_{1,0,12} - 11_{1,0,12}$	3.04*	54.82	1	-
220.7472403	CH$_3$CN	$12_{0,0,12} - 11_{0,0,12}$	3.04*	47.68	1	-
220.8106418	CH$_3$OCHO-A	$24_{1,23} - 24_{0,24}$	0.14	168.81	1	-
220.8117404	CH$_3$OCHO-E	$18_{3,15} - 17_{4,14}$	0.65	105.87	1	-
220.8140200	CH$_3$OCHO-E	$28_{5,23} - 28_{4,25}$	0.62	247.74	1	-
220.8151931	CH$_3$OCHO-A	$18_{3,16} - 17_{2,15}$	0.65	105.86	1	-
220.8476425	CH$_3$OCH$_3$	$24_{4,20,0} - 23_{5,19,0}$	1.84*	276.29	B	+
220.8889464	CH$_3$OCHO-A	$18_{17,1} - 17_{17,0}$	1.01*	271.32	1	-
220.8932375	CH$_3$OCH$_3$	$23_{4,20,2} - 23_{3,21,2}$	2.37*	253.23	B	-
220.9261742	CH$_3$OCHO-A	$18_{16,2} - 17_{16,1}$	1.30*	249.44	1	-
220.9351812	CH$_3$OCHO-E	$18_{16,2} - 17_{16,1}$	1.00	270.64	1	-
220.9468249	CH$_3$OCHO-A	$37_{9,29} - 37_{8,30}$	1.02	473.29	1	-
220.9475069	CH$_3$OCHO-E	$18_{16,3} - 17_{16,2}$	1.00	270.63	1	-
220.9615825	C$_2$H$_5$CN	$46_{6,40} - 46_{5,41}$	1.63	505.97	1	-
220.9625105	(CH$_3$)$_2$CO	$11_{11,1,0} - 10_{10,0,0}$	3.14*	41.74	1	-
220.9778206	CH$_3$OCHO-A	$18_{15,3} - 17_{15,2}$	1.47*	228.89	1	-
220.9785217	CH$_3$CN	$12_{9,1,12} - 11_{9,1,11}$	2.49*	1291.48	1	-
220.9834922	CH$_3$OCHO-E	$18_{15,3} - 17_{15,2}$	1.17	250.09	1	-
220.9872199	^{33}SO$_2$	$14_{3,11,13} - 14_{2,12,13}$	1.97*	97.31	1	-
220.9983979	CH$_3$OCHO-E	$18_{15,4} - 17_{15,3}$	1.17	250.08	1	-
220.9988850	C$_2$H$_5$OH	$13_{0,13,1} - 12_{0,12,1}$	1.32	135.54	1	-
221.0476595	CH$_3$OCHO-A	$18_{14,4} - 17_{14,3}$	1.58*	209.65	1	-
221.0498464	CH$_3$OCHO-E	$18_{14,4} - 17_{14,3}$	1.28	230.87	1	-
221.0516320	C$_2$H$_5$OH	$29_{7,22,0} - 29_{6,24,1}$	1.23	478.72	1	-
221.0669592	CH$_3$OCHO-E	$18_{14,5} - 17_{14,4}$	1.28	230.85	B	-
221.1148971	^{34}SO$_2$	$22_{2,20} - 22_{1,21}$	1.53	247.83	A	+
221.1396461	CH$_3$OCHO-E	$18_{13,5} - 17_{13,4}$	1.36	212.97	1	-
221.1410146	CH$_3$OCHO-A	$18_{13,5} - 17_{13,4}$	1.66*	191.74	1	-
221.1543046	C$_2$H$_5$OH	$29_{17,12,0} - 30_{16,14,1}$	0.57*	750.57	1	-
221.1585432	CH$_3$OCHO-E	$18_{13,6} - 17_{13,5}$	1.36	212.95	1	-
221.1770778	HDCS	$7_{1,6} - 6_{1,5}$	1.27	51.45	1	+
221.1916648	D$_2$CO	$4_{1,4} - 3_{1,3}$	1.31	31.96	1	-
221.1966270	CH$_3$CN	$12_{6,1,12} - 11_{6,1,12}$	2.89*	909.71	1	-
221.1978221	CH$_3$OCH$_3$	$27_{5,22,0} - 27_{4,23,0}$	2.61*	359.34	1	-
221.1991513	CH$_3$CN	$12_{-1,2,12} - 11_{1,2,12}$	3.01*	566.77	1	-
221.2020390	C$_2$H$_5$CN	$42_{2,40} - 42_{2,41}$	0.53	396.30	1	-
221.2158030	CH$_3$CHO	$11_{2,10,7} - 10_{2,9,7}$	2.09	450.75	B	-
221.2606831	CH$_3$OCHO-E	$18_{12,6} - 17_{12,5}$	1.42	196.40	1	-
221.2656015	CH$_3$OCHO-A	$18_{12,6} - 17_{12,5}$	1.73*	175.16	1	-
221.2727950	CH$_2$CN	$11_{3,9,12} - 10_{3,8,11}$	-2.64*	161.17	1	-
221.2748271	CH$_2$CN	$11_{2,10,11} - 10_{2,9,10}$	-2.39	116.52	1	-
221.2809035	CH$_3$OCHO-E	$18_{12,7} - 17_{12,6}$	1.42	196.39	1	-
221.2852410	^{13}CH$_3$OH	$8_{1,8} - 7_{0,7}(A-)$	0.70	87.12	1	-
221.2938400	CH$_3$OCHO-E	$28_{6,23} - 28_{5,24}$	0.62	247.76	1	-
221.2958080	CH$_3$CHO	$13_{3,10,0} - 13_{2,11,0}$	1.22	104.69	1	-
221.3119500	CH$_3$CN	$12_{6,2,12} - 11_{6,2,12}$	2.89*	749.85	1	+
221.3382190	CH$_3$CN	$12_{3,1,12} - 11_{3,1,12}$	2.98*	677.15	1	+
221.3503700	CH$_3$CN	$12_{5,2,12} - 11_{5,2,12}$	2.93*	684.78	1	+
221.3676691	CH$_3$CN	$12_{2,1,12} - 11_{2,1,12}$	3.30*	628.15	1	+
221.3807396	CH$_3$CN	$12_{4,2,12} - 11_{4,2,12}$	3.26*	633.92	1	-

Table A.1. continued.

Frequency	Molecule	Transition	$\log(\mu^2 S)^a$	E_u [K]^b	Flag^c	Plot^d
221.3873001	CH$_3$CN	$12_{1,1,12} - 11_{1,1,12}$	3.01*	593.42	1	-
221.3941500	CH$_3$CN	$12_{0,2,12} - 11_{0,2,12}$	3.01*	572.98	1	-
225.5990847	CH$_3$OCH$_3$	$12_{1,12,2} - 11_{0,11,2}$	2.34*	48.13	1	-
225.6977750	H$_2$CO	$3_{1,2} - 2_{1,1}$	1.64	33.45	1	+
225.8967200	HDO	$3_{1,2} - 2_{2,1}$	-0.16	167.56	1	+
226.2563101	CH$_3$CHO	$13_{0,13,0} - 12_{1,12,0}$	1.31	83.05	B	-
226.3000267	SO$_2$	$14_{3,11} - 14_{2,12}$	1.36	118.98	A	-
226.3469275	CH$_3$OCH$_3$	$14_{1,13,0} - 13_{2,12,0}$	2.00*	77.14	1	-
226.5383379	(CH$_3$)$_2$CO	$8_{8,1,1} - 7_{5,3,2}$	-0.49	34.10	A	-
226.7846543	(CH$_3$)$_2$CO	$20_{3,17,1} - 19_{4,16,1}$	3.34*	104.67	A	-
226.8126092	(CH$_3$)$_2$CO	$12_{9,3,0} - 11_{8,4,1}$	2.74	66.19	A	-
226.8577140	CH$_3$CHO	$11_{3,8,2} - 11_{2,9,2}$	0.99	81.48	B	-
227.0194892	CH$_3$OCHO-E	$19_{4,16} - 18_{4,15}$	1.69	116.57	1	-
227.0280673	CH$_3$OCHO-A	$19_{2,17} - 18_{2,16}$	1.69	116.56	1	-
227.0318807	^{34}SO$_2$	$12_{3,9} - 12_{2,10}$	1.27	93.08	1	-
227.0946010	CH$_3$OH	$21_{1,20} - 21_{0,21}(A+)$	1.06	557.06	1	-
227.1141731	D$_2$CS	$8_{5,3} - 7_{5,2}$	1.43*	185.69	1	+
227.1799845	D$_2$CS	$8_{4,4} - 7_{4,3}$	1.82*	128.69	1	+
227.4189050	HC$_3$N	$25 - 24$	2.54	141.89	A	+
227.5143590	CH$_3$CHO	$11_{3,8,0} - 11_{2,9,0}$	1.13	81.49	B	-
227.5613486	CH$_3$OCHO-E	$21_{2,20} - 20_{1,20}$	2.11*	100.58	1	-|
227.5622413	CH$_3$OCHO-A	$21_{0,21} - 20_{1,20}$	2.08*	100.56	1	-|
229.4320840	CH$_3$CHO	$11_{1,11,1} - 10_{0,10,2}$	1.23	61.54	B	-
229.5591486	C$_2$H$_5$OH	$14_{0,14,1} - 13_{1,13,1}$	-1.15	146.39	A	-
229.5890730	CH$_3$OH	$15_{4,11} - 16_{3,13}(A+)$	0.66	374.43	1	-|
229.5904100	CH$_3$OCHO-E	$19_{3,16} - 18_{4,15}$	0.70	116.69	1	-|
229.5950200	CH$_3$OCHO-A	$19_{3,17} - 18_{2,16}$	0.70	116.68	1	-
229.7587600	CH$_3$OH	$8_{1,8} - 7_{0,7}(A-)$	0.70	89.10	1	-
229.7750710	CH$_3$CHO	$11_{1,11,0} - 10_{0,10,0}$	1.23	61.46	B	-
229.8548654	SO^{18}O	$14_{0,14} - 13_{1,13}$	1.44	88.85	A	-
229.8576282	^{34}SO$_2$	$4_{2,2} - 3_{1,3}$	0.66	18.67	1	-
229.8609140	CH$_3$CHO	$10_{3,7,0} - 10_{2,8,0}$	1.08	71.29	B	-
229.8641900	CH$_3$OH	$19_{5,15} - 20_{4,16}(+E)$	0.76	578.59	1	-
229.9391800	CH$_3$OH	$19_{5,14} - 20_{4,17}(-E)$	0.76	578.59	1	-
230.0270600	CH$_3$OH	$3_{2,2} - 4_{1,4}(A-)$	-0.13	39.83	1	-
230.1055541	CH$_3$CHO	$26_{3,23,2} - 25_{4,22,1}$	1.02	348.36	1	-|
230.1066085	CH$_3$CHO	$12_{2,10,5} - 12_{1,12,4}$	0.20	287.68	1	-|
230.1084450	C$_2$H$_5$OH	$43_{5,38,0} - 43_{4,39,0}$	-0.63	885.64	1	-|
230.1413735	CH$_3$OCH$_3$	$25_{4,22,2} - 25_{3,22,2}$	2.40*	297.12	1	-
230.1446090	CH$_3$CHO	$13_{0,13,3} - 12_{1,12,3}$	1.27	289.71	B	-
230.1595183	CH$_3$OCHO-E	$35_{10,26} - 35_{0,35}$	0.41	418.81	1	-
230.1777310	(CH$_3$)$_2$CO	$23_{0,23,0} - 22_{0,22,1}$	3.86*	112.86	1	-
230.1828134	(CH$_3$)$_2$CO	$28_{2,26,0} - 28_{2,27,1}$	2.81*	197.70	1	-
230.2314190	SO^{17}O	$13_{3,10} - 13_{2,11}$	2.09	103.28	1	-
230.2337575	CH$_3$OCH$_3$	$17_{2,15,0} - 16_{3,14,0}$	1.96*	125.55	1	-
230.2728523	CH$_3$CHO	$9_{5,4,2} - 10_{4,7,1}$	0.24	98.01	B	-
230.2927250	CH$_3$OH	$22_{2,20} - 21_{3,19}(A+)$	0.00	609.54	1	-|
230.2938579	CH$_3$OCHO-A	$22_{9,13} - 22_{8,14}$	0.71	203.35	1	-|
230.3018800	CH$_3$CHO	$12_{2,11,0} - 11_{2,10,0}$	2.17	81.04	B	-
230.3157400	CH$_3$CHO	$12_{2,11,1} - 11_{2,10,1}$	2.17	81.05	B	-|
230.3175270	O^{13}CS	$19 - 18$	0.99	110.54	1	-|
230.3681785	CH$_3$OCH$_3$	$28_{5,23,3} - 27_{6,22,3}$	1.90*	384.23	1	-|
230.3681990	CH$_3$OH	$22_{4,18} - 21_{5,17}(A+)$	0.82	682.73	1	-|
230.3764780	CH$_3$OCHO-A	$22_{9,14} - 22_{8,15}$	0.71	203.35	1	-|
230.3780799	C$_2$H$_5$OH	$11_{5,6,1} - 11_{4,7,1}$	-1.28	147.18	1	-|
230.3951700	CH$_3$CHO	$12_{2,11,3} - 11_{2,10,3}$	2.17	286.40	B	-
230.4531157	CH$_3$CHO	$8_{3,6,1} - 8_{2,6,2}$	0.32	53.60	B	-
230.5075159	CH$_3$OCH$_3$	$26_{4,23,0} - 25_{5,20,0}$	1.95*	320.83	1	+
230.5380000	CO	$2 - 1$	-1.62	16.60	1	+
230.6010400	CH$_3$CHO	$5_{2,4,1} - 4_{1,3,2}$	0.44	22.91	B	-
230.6725540	C$_2$H$_5$OH	$13_{2,11,0} - 12_{2,10,0}$	1.31	138.62	B	-
230.6915910	D$_2$CO	$13_{2,11} - 13_{2,12}$	0.71	285.49	1	-
230.8108827	SO^{17}O	$14_{2,13} - 14_{1,14}$	1.92	102.83	1	+
230.9271460	CH$_3$CHO	$12_{6,6,5} - 11_{6,5,5}$	2.06	359.36	B	-

Table A.1. continued.

Frequency	Molecule	Transition	$\log(\mu^2 S)^a$	E_u [K][b]	Flag[c]	Plot[d]
230.9363200	CH$_3$OCHO-E	$29_{5,24} - 29_{4,26}$	0.62	264.14	1	-
231.0609934	OCS	$19 - 18$	0.99	110.90	1	+
231.1142580	CH$_3$CHO	$9_{3,6,2} - 9_{2,7,2}$	0.88	62.03	B	-
231.1165900	CH$_3$CHO	$12_{8,4,3} - 11_{8,3,3}$	2.23*	399.27	B	-
231.1494163	CH$_3$CHO	$12_{11,1,2} - 11_{11,0,2}$	1.39	344.56	B	-|
231.1502100	CH$_3$CHO	$12_{4,8,5} - 11_{4,7,5}$	2.13	314.33	B	-|
231.1728105	(CH$_3$)$_2$CO	$12_{10,2,0} - 11_{9,3,1}$	1.45	68.58	A	+
231.1835600	CH$_3$CHO	$12_{9,3,2} - 11_{9,2,2}$	1.82	254.62	B	-|
231.1854280	CH$_3$CHO	$12_{10,3,1} - 11_{10,2,1}$	1.67	297.30	B	-|
231.1953200	CH$_3$CHO	$12_{8,4,2} - 11_{8,3,2}$	1.93	216.40	B	-|
231.1953200	CH$_3$CHO	$12_{9,4,1} - 11_{9,3,1}$	1.82	254.61	B	-|
231.1992628	CH$_3$OCHO-A	$21_{9,12} - 21_{8,13}$	0.68	190.29	1	-|
231.2000431	CH$_3$CHO	$12_{8,4,5} - 11_{8,3,5}$	1.93	420.75	B	-|
231.2001400	CH$_3$OCHO-E	$21_{9,12} - 21_{8,13}$	0.68	190.29	1	-|
231.2126600	CH$_3$CHO	$12_{10,2,0} - 11_{10,1,0}$	1.97*	275.06	B	-
231.2206852	^{13}CS	$5_0 - 4_0$	1.58	33.29	1	+
231.2254500	CH$_3$CHO	$12_{7,5,2} - 11_{7,4,2}$	2.00	182.64	B	-|
231.2269550	CH$_3$CHO	$12_{9,3,0} - 11_{9,2,0}$	2.12*	232.33	B	-|
231.2336498	CH$_3$CHO	$12_{8,5,1} - 11_{8,4,1}$	2.40*	194.11	B	-
231.2449800	CH$_3$CHO	$12_{7,5,0} - 11_{7,4,0}$	2.30*	160.38	B	-
231.2557700	CH$_3$CHO	$12_{5,7,5} - 11_{5,6,5}$	2.10	334.37	B	-
231.2676400	CH$_3$CHO	$12_{7,6,1} - 11_{7,5,1}$	2.00	182.53	B	-
231.2729582	CH$_3$CHO	$12_{6,7,0} - 11_{6,6,0}$	2.53*	131.15	B	-
231.2811000	CH$_3$OH	$10_{2,9} - 9_{3,6}(-E)$	0.43	165.34	1	-
231.3104600	CH$_3$CHO	$12_{6,7,1} - 11_{6,6,1}$	2.06	153.26	B	-|
231.3104889	CH$_3$CHO	$7_{3,5,1} - 7_{2,5,2}$	0.05	46.19	B	-|
231.3122995	C$_2$H$_5$CN	$27_{0,27} - 26_{1,26}$	1.54	157.70	A	-|
231.3132402	C$_2$H$_5$CN	$24_{2,23} - 23_{1,22}$	1.26	132.43	A	-|
231.3218566	N$_2$D$^+$	$3 - 2$	2.49	22.20	1	+
231.3297000	CH$_3$CHO	$12_{5,8,0} - 11_{5,7,0}$	2.40*	106.41	B	-
231.3572900	CH$_3$CHO	$12_{3,9,5} - 11_{3,8,5}$	2.15	299.05	B	-
231.3665150	CH$_3$CHO	$12_{5,7,2} - 11_{5,6,2}$	2.40*	106.32	B	-
231.3820710	CH$_3$CHO	$12_{5,8,4} - 11_{5,7,4}$	2.10	333.58	B	-
231.3892035	(CH$_3$)$_2$CO	$9_{3,7,0} - 8_{0,8,1}$	0.97	29.85	A	+
336.8651100	CH$_3$OH	$12_{1,11} - 12_{0,12}(-E)$	1.36	197.07	1	+
336.8892125	CH$_3$OCHO-E	$26_{0,26} - 25_{0,25}$	1.82	235.46	1	+
336.9180949	CH$_3$OCHO-A	$26_{6,20} - 25_{6,19}$	1.82	235.46	1	+
336.9421799	(CH$_3$)$_2$CO	$24_{11,13,0} - 23_{12,12,0}$	2.73	230.39	1	-
336.9476895	(CH$_3$)$_2$CO	$33_{1,32,1} - 32_{2,31,2}$	3.63*	252.63	1	-
336.9532380	C$_2$H$_5$CN	$51_{8,43} - 51_{7,44}$	1.63	641.69	1	-
337.0266138	SO^{18}O	$27_{9,18} - 28_{8,21}$	1.26*	489.73	A	+
337.0547330	CH$_3$CHO	$18_{8,10,8} - 17_{8,9,8}$	2.29	692.10	B	-
337.0611207	C^{17}O	$3_1 - 2_1$	-0.66*	0.00	1	-
337.0810820	CH$_3$CHO	$18_{1,18,6} - 17_{1,17,6}$	2.34	526.12	B	-
337.1358730	CH$_3$OH	$3_{3,0} - 4_{2,2}(A+)$	-0.61	61.64	1	-|
337.1363180	CH$_3$OCHO-E	$36_{3,34} - 36_{1,36}$	0.65*	331.03	1	-|
337.1844552	CH$_3$OCH$_3$	$31_{3,28,3} - 31_{0,31,3}$	1.94*	415.16	1	-
337.1872764	CH$_3$CHO	$24_{2,22,3} - 23_{3,21,3}$	1.11	496.77	B	-|
337.1889589	CH$_3$OCH$_3$	$31_{3,28,0} - 31_{0,31,0}$	1.94*	415.16	1	-|
337.1984253	^{33}SO	$8_{7,6} - 7_{6,5}$	1.80*	48.17	1	-
337.2417130	CH$_3$CHO	$12_{2,11,1} - 11_{1,10,2}$	0.99	81.05	B	-
337.2496124	^{33}SO	$8_{7,6} - 7_{6,6}$	0.22*	48.16	1	-
337.2784481	(CH$_3$)$_2$CO	$41_{25,16,0} - 40_{28,13,1}$	1.14	700.82	1	-
337.2862444	(CH$_3$)$_2$CO	$36_{32,5,0} - 35_{33,3,1}$	1.36	606.30	1	-
337.2970681	CH$_3$OCH$_3$	$43_{8,36,0} - 42_{9,33,0}$	2.08*	920.41	1	-|
337.2974390	CH$_3$OH	$7_{1,7} - 6_{1,6}, v = 1(+E)$	0.74	390.01	1	-|
337.3010067	CH$_3$OCHO-A	$36_{1,35} - 36_{1,36}$	0.65*	331.00	1	-|
337.3025736	NH$_2$CHO	$19_{2,18,19} - 19_{1,19,19}$	1.12*	171.60	1	-|
337.3047696	^{33}SO	$8_{7,7} - 7_{6,8}$	-2.32	80.53	1	-
337.3230950	C$_2$H$_5$OH	$20_{7,14,2} - 20_{6,15,2}$	1.29	238.01	1	-
337.3475840	C$_2$H$_5$CN	$38_{3,36} - 37_{3,35}$	2.75	327.85	1	-
337.3678544	CH$_2$DCN	$2_{2,1} - 2_{1,2}$	-1.60	24.07	1	-
337.3744549	CH$_3$CHO	$26_{4,23,0} - 26_{3,24,0}$	1.52	361.51	B	-

Table A.1. continued.

Frequency	Molecule	Transition	$\log(\mu^2 S)^a$	$E_{\rm u}$ [K]^b	Flag^c	Plot^d
337.3964590	C^{34}S	$7_0 - 6_0$	1.43	64.77	1	+
337.4213396	CH$_3$OCH$_3$	$21_{2,19,0} - 20_{3,18,0}$	2.18*	187.75	1	+
337.4435631	HCOOH	$15_{8,8} - 14_{8,7}$	1.62*	300.36	1	+
337.4636710	CH$_3$OH	$7_{6,1} - 6_{6,0}, v = 1(+E)$	0.48*	500.61	1	-
337.4666253	C$_2$H$_5$CN	$13_{6,8} - 14_{4,11}$	-2.41	79.14	A	-
337.4747690	H$_2$C^{34}S	$10_{2,9} - 9_{2,8}$	1.42	141.82	A	+
337.4899220	CH$_3$CHO	$28_{3,26,0} - 28_{1,27,0}$	0.31	396.09	B	-|
337.4905230	CH$_3$OH	$7_{6,2} - 6_{6,1}, v = 1(A-)$	0.16	558.23	1	-|
337.5034508	CH$_3$OCHO-A	$27_{8,20} - 26_{8,19}$	1.82	267.09	1	+
337.5190670	CH$_3$OH	$7_{3,5} - 6_{3,4}, v = 1(A+)$	0.66	482.22	1	+
337.5460480	CH$_3$OH	$7_{5,3} - 6_{5,2}, v = 1(+E)$	0.74*	452.95	1	-
337.5516472	D$_2$^{13}CO	$6_{0,6} - 5_{0,5}$	1.82	57.25	1	+
337.5816630	CH$_3$OH	$7_{4,4} - 6_{4,3}, v = 1(A+)$	0.58	428.19	1	+
337.5986450	D$_2$CS	$12_{0,12} - 11_{0,11}$	1.82	105.77	1	-
337.6052550	CH$_3$OH	$7_{2,5} - 6_{2,4}, v = 1(A-)$	0.72	429.42	1	-
337.6105800	CH$_3$OH	$7_{6,1} - 6_{6,0}, v = 1(A+)$	0.16	657.10	1	-|
337.6106240	CH$_3$OH	$7_{3,4} - 6_{3,3}, v = 1(A-)$	0.66	387.44	1	-|
337.6107293	CH$_3$^{13}CH$_2$CN	$10_{6,5} - 9_{5,4}$	1.82*	30.14	1	-|
337.6306670	CH$_3$OH	$7_{2,5} - 6_{2,4}, v = 1(+E)$	1.02*	331.08	1	+
337.6423650	CH$_3$OH	$7_{1,7} - 6_{1,6}, v = 1(A+)$	0.74	356.29	1	-|
337.6438640	CH$_3$OH	$7_{0,7} - 6_{0,6}, v = 1(A+)$	0.75	365.39	1	-|
337.6459920	CH$_3$OH	$7_{4,3} - 6_{4,2}, v = 1(A-)$	0.58	470.21	1	-
337.6481670	CH$_3$OH	$7_{5,3} - 6_{5,2}, v = 1(A-)$	0.44	610.95	1	-
337.6552040	CH$_3$OH	$7_{3,5} - 6_{3,4}, v = 1(+E)$	0.97*	428.52	1	+
337.6711940	CH$_3$OH	$7_{2,6} - 6_{2,5}, v = 1(A+)$	0.72	464.71	1	+
337.6854900	CH$_3$OH	$7_{4,3} - 6_{4,2}, v = 1(+E)$	0.88*	513.47	1	-|
337.6854900	CH$_3$OH	$7_{5,2} - 6_{5,1}, v = 1(A+)$	0.44	493.94	1	-|
337.7075470	CH$_3$OH	$7_{1,6} - 6_{1,5}, v = 1(A-)$	0.74	478.20	1	-|
337.7086296	CH$_3$OCH$_3$	$31_{2,30,3} - 31_{1,31,3}$	1.31*	415.14	1	-|
337.7207678	CH$_3$OCH$_3$	$7_{4,4,2} - 6_{3,3,2}$	1.38*	15.57	B	-
337.7270950	C$_2$H$_5$OH	$19_{7,12,2} - 19_{6,13,2}$	1.27	221.18	1	-|
337.7281852	CH$_3$OCH$_3$	$7_{4,4,3} - 6_{3,3,3}$	1.83*	15.57	1	-|
337.7487830	CH$_3$OH	$7_{0,7} - 6_{0,6}, v = 1(+E)$	0.75	488.48	1	+
337.7711578	CH$_3$OCHO-A	$44_{5,39} - 44_{4,40}$	0.84	604.33	B	-
337.7774213	CH$_3$OCH$_3$	$7_{4,4,2} - 6_{3,4,2}$	1.63*	15.56	B	-
337.7838926	CH$_3$OCH$_3$	$7_{4,3,0} - 6_{3,4,0}$	1.93*	15.56	1	+
337.8010704	C$_2$H$_5$OH	$19_{2,17,0} - 18_{2,16,0}$	1.48	223.08	1	-
337.8371156	C$_2$H$_5$OH	$11_{11,1,2} - 12_{10,2,2}$	-1.05	207.07	A	-|
337.8380890	CH$_3$OH	$20_{6,14} - 21_{5,16}(A-)$	0.74	675.93	1	-|
337.8661646	CH$_3$CHO	$20_{1,19,3} - 19_{2,18,3}$	1.26	405.45	B	-
337.8776218	(CH$_3$)$_2$CO	$34_{28,7,0} - 33_{29,4,0}$	1.78*	491.76	1	-
337.8833340	CH$_3$CHO	$17_{1,16,6} - 16_{1,15,6}$	2.31	518.52	B	-
337.8922466	^{34}SO	$3_3 - 2_3$	-0.66	25.31	A	+
337.9063211	C$_2$H$_5$OH	$42_{3,39,0} - 41_{4,37,1}$	1.03	824.46	B	-
337.9694140	CH$_3$OH	$7_{1,6} - 6_{1,5}, v = 1(-E)$	0.74	390.14	1	+
338.0831953	H$_2$CS	$10_{1,10} - 9_{1,9}$	1.91	102.43	1	+
338.0992570	C$_2$H$_5$OH	$18_{7,11,2} - 18_{6,12,2}$	1.24	205.19	1	-
338.1052800	CH$_3$CHO	$5_{3,2,5} - 4_{2,2,5}$	0.80	240.80	B	-|
338.1071430	(CH$_3$)$_2$CO	$34_{0,34,0} - 33_{1,33,1}$	4.14*	255.08	1	-|
338.1096730	C$_2$H$_5$OH	$18_{7,12,2} - 18_{6,13,2}$	1.24	205.19	1	-
338.1176487	(CH$_3$)$_2$CO	$26_{9,17,0} - 25_{10,16,1}$	3.61*	218.71	1	-
338.1245020	CH$_3$OH	$7_{0,7} - 6_{0,6}(A+)$	0.75	78.08	1	-
338.1428510	C$_2$H$_5$CN	$37_{3,34} - 36_{3,33}$	2.74	316.76	A	-
338.2620170	CH$_2$DCN	$5_{2,4} - 5_{1,5}$	-1.11	34.08	B	-
338.2995240	CH$_3$CHO	$12_{2,11,0} - 11_{1,10,0}$	1.00	81.04	B	-
338.3059931	SO$_2$	$18_{4,14} - 18_{3,15}$	1.43	196.79	1	-
338.3182717	(CH$_3$)$_2$CO	$34_{25,10,1} - 34_{22,13,2}$	0.62	503.70	1	-
338.3203564	^{34}SO$_2$	$13_{2,12} - 12_{1,11}$	1.13	92.45	A	-
338.3380143	CH$_3$OCHO-E	$27_{8,19} - 26_{8,18}$	1.82	267.18	B	-
338.3446280	CH$_3$OH	$7_{1,7} - 6_{1,6}(A-)$	0.74	70.55	1	-
338.3557715	CH$_3$OCHO-A	$27_{8,19} - 26_{8,18}$	1.82	267.18	B	+
338.3963889	CH$_3$OCHO-E	$27_{7,21} - 26_{7,20}$	1.83	257.74	B	+
338.4045800	CH$_3$OH	$7_{6,2} - 6_{6,1}(A+)$	0.17	243.78	1	-
338.4086810	CH$_3$OH	$7_{0,7} - 6_{0,6}(+E)$	0.75	64.98	1	-

Table A.1. continued.

Frequency	Molecule	Transition	$\log(\mu^2 S)^a$	E_u [K]^b	Flag^c	Plot^d
338.4140995	CH$_3$OCHO-A	$27_{7,21} - 26_{7,20}$	1.83	257.74	B	-
338.4168741	C$_2$H$_5$OH	$17_{7,11,2} - 17_{6,12,2}$	1.21	190.04	1	-
338.4309330	CH$_3$OH	$7_{6,1} - 6_{6,0}(A-)$	0.18	253.94	1	+
338.4423440	CH$_3$OH	$7_{6,1} - 6_{6,0}(+E)$	0.48*	226.21	1	+
338.4564990	CH$_3$OH	$7_{5,2} - 6_{5,1}(A-)$	0.44	188.99	1	+
338.4752900	CH$_3$OH	$7_{5,3} - 6_{5,2}(A+)$	0.44	201.05	1	+
338.4863370	CH$_3$OH	$7_{5,3} - 6_{5,2}(+E)$	0.74*	170.39	1	+
338.5040990	CH$_3$OH	$7_{4,4} - 6_{4,3}(A-)$	0.58	152.89	1	+
338.5126330	CH$_3$OH	$7_{4,4} - 6_{4,3}(-E)$	0.88*	112.84	1	-⎫
338.5128560	CH$_3$OH	$7_{2,6} - 6_{2,5}(-E)$	0.72	102.70	1	-⎭
338.5272488	^{33}SO	$3_{3,5} - 2_{3,5}$	-0.54	25.41	A	-
338.5302490	CH$_3$OH	$7_{4,3} - 6_{4,2}(A+)$	0.58	160.99	1	-
338.5419995	CH$_3$OH	$7_{3,5} - 6_{3,4}(+E)$	0.96*	82.30	1	+
338.5599280	CH$_3$OH	$7_{3,5} - 6_{3,4}(A-)$	0.67	127.70	1	+
338.5831950	CH$_3$OH	$7_{3,4} - 6_{3,3}(A+)$	0.66	112.71	1	+
338.6118103	SO$_2$	$20_{1,19} - 19_{2,18}$	1.42	198.87	1	-
338.6149990	CH$_3$OH	$7_{1,6} - 6_{1,5}(A+)$	0.75	86.05	1	-
338.6399390	CH$_3$OH	$7_{2,5} - 6_{2,4}(+E)$	0.72	102.71	1	+
338.6729900	C$_2$H$_5$OH	$16_{7,9,2} - 16_{6,10,2}$	1.47*	143.23	1	-
338.7216300	CH$_3$OH	$7_{2,5} - 6_{2,4}(A+)$	0.71	87.26	1	-⎫
338.7229400	CH$_3$OH	$7_{2,6} - 6_{2,5}(A-)$	0.72	90.91	1	-⎭
1289.05	C$_2$H$_5$OH	$52_{8,45,1} - 52_{7,45,0}$	1.49	******	B	-
338.7400994	C$_2$H$_5$OH	$36_{6,30,2} - 35_{7,29,2}$	1.11	608.82	1	-
338.7486806	C$_2$H$_5$CN	$23_{7,16} - 24_{5,19}$	-1.70	173.13	B	-
341.1316650	^{13}CH$_3$OH	$13_{1,12} - 13_{0,13}(-E)$	1.39	222.31	1	-
341.2755244	SO$_2$	$21_{8,14} - 22_{7,15}$	0.80	369.13	A	+
341.3502290	HCS$^+$	$8 - 7$	1.49	73.72	A	+
341.4156390	CH$_3$OH	$7_{1,6} - 6_{1,5}(-E)$	0.74	80.09	1	-
341.4649300	CH$_3$CHO	$18_{1,18,1} - 17_{0,17,2}$	1.51	155.22	B	-
341.6150200	CH$_3$CHO	$18_{1,18,0} - 17_{0,17,0}$	1.51	155.15	B	-
341.6739613	SO$_2$	$36_{5,31} - 36_{4,32}$	1.83	678.50	A	+
341.7247312	^{33}SO$_2$	$13_{2,12,12} - 12_{1,11,11}$	1.73*	59.91	A	+
341.7323005	CH$_3$OCHO-A	$29_{4,26} - 28_{4,25}$	1.87	264.16	B	-
341.9181187	CH$_3$OCHO-E	$29_{5,24} - 28_{5,23}$	1.87	264.14	1	-
341.9272670	C$_2$H$_5$CN	$20_{4,16} - 19_{3,17}$	0.96	108.18	B	-⎫
341.9275081	CH$_3$OCHO-A	$29_{3,26} - 28_{3,25}$	1.87	264.14	B	-⎭
342.2300972	CH$_3$OCHO-E	$29_{6,24} - 28_{5,23}$	0.91	264.16	A	-
342.3551031	CH$_3$OCHO-E	$30_{5,26} - 29_{5,25}$	2.19*	236.63	1	-
342.3596229	CH$_3$OCHO-E	$30_{5,26} - 29_{4,26}$	1.94*	236.63	1	-
342.3628322	CH$_3$OCHO-A	$30_{3,28} - 29_{3,27}$	2.19*	236.62	1	-
342.5221280	D$_2$CO	$6_{0,6} - 5_{0,5}$	1.81	58.12	1	-
342.5252977	CH$_3$OCHO-E	$11_{8,3} - 10_{7,3}$	0.54	81.42	1	-
342.5724154	CH$_3$OCHO-A	$11_{8,4} - 10_{7,3}$	0.84*	48.53	1	-
342.6081188	CH$_3$OCH$_3$	$19_{0,19,3} - 18_{1,18,3}$	2.59*	134.25	1	-
342.7298300	CH$_3$OH	$13_{1,12} - 13_{0,13}(-E)$	1.39	227.47	1	-
342.7616254	SO$_2$	$34_{3,31} - 34_{2,32}$	1.71	581.91	A	+
342.8828503	CS	$7_0 - 6_0$	1.43	65.83	1	+
342.9477426	CH$_3$OCH$_3$	$41_{3,39,0} - 41_{6,36,0}$	2.58*	788.63	1	-
342.9680977	CH$_3$OCHO-E	$12_{4,9} - 11_{1,10}$	-0.99	56.85	B	-
343.0875458	^{33}SO	$8_{9,10} - 7_{8,9}$	1.92*	45.10	1	+
346.8643205	C$_2$H$_5$CN	$22_{8,14} - 22_{7,15}$	1.49*	146.59	A	-
346.8679114	CH$_3$CHO	$18_{15,4,4} - 17_{15,3,4}$	1.84	864.58	B	-⎫
346.8691780	H$_2$C^{18}O	$5_{2,4} - 4_{2,3}$	1.36	97.40	1	-⎭
346.8934200	CH$_3$CHO	$18_{8,11,1} - 17_{8,10,1}$	2.74*	269.02	B	-
346.8982299	C$_2$H$_5$CN	$21_{8,13} - 21_{7,14}$	1.47*	137.13	A	-
346.9250899	C$_2$H$_5$CN	$20_{8,12} - 20_{7,13}$	1.44*	128.10	A	+
346.9342700	CH$_3$CHO	$18_{7,11,2} - 17_{7,10,2}$	2.29	268.65	B	-
346.9388742	C$_2$H$_5$OH	$20_{6,14,1} - 19_{6,13,1}$	1.46	280.47	A	-⎫
346.9406616	C$_2$H$_5$CN	$8_{8,0} - 8_{7,1}$	0.46*	53.29	A	-⎭
346.9456707	C$_2$H$_5$CN	$19_{8,11} - 19_{7,12}$	1.41*	119.49	A	-
346.9569520	C$_2$H$_5$CN	$10_{8,2} - 10_{7,3}$	0.90*	61.45	A	-⎫
346.9573800	CH$_3$CHO	$18_{7,12,0} - 17_{7,11,0}$	2.59*	235.30	B	-⎭
346.9607049	C$_2$H$_5$CN	$18_{8,10} - 18_{7,11}$	1.38*	111.32	A	-⎫
346.9612355	SO^{18}O	$9_{2,7} - 8_{1,8}$	0.69	48.98	A	-⎭

Table A.1. continued.

Frequency	Molecule	Transition	$\log(\mu^2 S)^a$	E_u [K]^b	Flag^c	Plot^d
346.9625940	C_2H_5OH	$21_{0,21,2} - 20_{1,20,2}$	1.33	185.84	1	-
346.9643632	C_2H_5CN	$11_{8,3} - 11_{7,4}$	1.01*	66.18	A	-|
346.9707599	C_2H_5CN	$12_{8,4} - 12_{7,5}$	1.09*	71.34	A	-
346.9708872	C_2H_5CN	$17_{8,9} - 17_{7,10}$	1.34*	103.58	A	-|
346.9745486	C_2H_5OH	$17_{3,15,0} - 16_{2,15,1}$	0.83	195.16	1	-
346.9757031	C_2H_5CN	$13_{8,5} - 13_{7,6}$	1.16*	76.93	A	-
346.9768755	C_2H_5CN	$16_{8,8} - 16_{7,9}$	1.31*	96.27	A	-
346.9773655	CH_3OCHO-A	$37_{1,36} - 37_{1,37}$	0.65*	349.59	1	-
346.9787172	C_2H_5CN	$14_{8,6} - 14_{7,7}$	1.21*	82.95	A	-
346.9792906	C_2H_5CN	$15_{8,7} - 15_{7,8}$	1.26*	89.39	A	-
346.9839750	$H_2C^{18}O$	$5_{4,1} - 4_{4,0}$	1.29*	206.26	1	-
346.9867973	HCOOD	$4_{3,2} - 5_{1,5}$	-3.62	34.29	A	-
346.9969700	CH_3CHO	$18_{7,12,1} - 17_{7,11,1}$	2.29	268.56	B	-|
346.9983440	$H^{13}CO^+$	$4 - 3$	1.78	41.63	1	+|
347.0434349	CH_2DCN	$20_{0,20} - 19_{0,19}$	2.49	174.95	1	+
347.0716400	CH_3CHO	$18_{6,13,0} - 17_{6,12,0}$	2.61*	206.08	1	+
347.0899400	CH_3CHO	$18_{6,12,2} - 17_{6,11,2}$	2.31	239.39	1	+
347.1101228	CH_2DCN	$20_{5,15} - 19_{5,14}$	2.76*	276.41	1	+
347.1177162	CH_3CHO	$18_{12,6,3} - 17_{12,5,3}$	2.40*	650.97	B	+
347.1326859	CH_3CHO	$18_{6,13,1} - 17_{6,12,1}$	2.31	239.31	B	-|
347.1338640	$H_2C^{18}O$	$5_{3,3} - 4_{3,2}$	1.72	156.69	B	-|
347.1440112	$H_2C^{18}O$	$5_{3,2} - 4_{3,1}$	1.72	156.69	B	-
347.1472094	C_2H_5OH	$20_{6,15,0} - 19_{6,14,0}$	1.46	275.45	A	-
347.1551248	CH_3CHO	$18_{4,14,8} - 17_{4,13,8}$	2.33	573.91	B	-|
347.1557752	CH_3CHO	$9_{4,6,4} - 9_{3,7,4}$	0.99	282.77	B	-|
347.1579974	C_2H_5OH	$20_{6,14,0} - 19_{6,13,0}$	1.46	275.45	1	-
347.1618629	C_2H_5OH	$21_{1,21,2} - 20_{1,20,2}$	-1.35	185.85	A	-
347.1664788	CH_2DCN	$20_{4,17} - 19_{4,16}$	2.77*	227.92	1	-
347.1695196	CH_3CHO	$19_{0,19,0} - 18_{1,18,0}$	1.54	171.81	B	-
347.1819200	CH_3CHO	$18_{4,14,5} - 17_{4,13,5}$	2.34	400.37	B	-
347.1882830	$^{13}CH_3OH$	$14_{1,13} - 14_{0,14}(-E)$	1.41	254.25	1	-|
347.1882949	CH_2DCN	$20_{2,19} - 19_{2,18}$	2.48	196.56	1	-|
347.2176900	CH_3CHO	$18_{5,13,5} - 17_{5,12,5}$	2.32	420.43	B	-|
347.2181534	CH_2DCN	$20_{3,18} - 19_{3,17}$	2.78*	190.20	1	-|
347.2234438	CH_3OCH_3	$10_{10,1,0} - 11_{9,2,0}$	0.29*	157.22	1	-
347.2403963	CH_3CHO	$19_{0,19,2} - 18_{1,18,1}$	1.54	171.88	B	+
347.2518220	CH_3CHO	$18_{5,14,4} - 17_{5,13,4}$	2.32	419.66	B	+
347.2915691	CH_3CHO	$18_{5,14,0} - 17_{5,13,0}$	2.62*	181.36	B	+
347.3306310	SiO	$8 - 7$	1.89	75.02	1	+
347.3470563	CH_3OCH_3	$37_{7,30,0} - 36_{6,31,0}$	2.58*	677.04	1	-|
347.3474946	CH_3CHO	$18_{5,13,2} - 17_{5,12,2}$	2.62*	181.28	B	-|
347.3509290	C_2H_5OH	$14_{3,12,2} - 13_{2,11,2}$	1.02	99.66	A	-
347.3702042	C_2H_5OH	$34_{4,30,0} - 33_{5,28,1}$	0.89	579.09	1	+
347.3882105	CH_2DCN	$20_{2,18} - 19_{2,17}$	2.48	196.61	1	+
347.4455230	C_2H_5OH	$21_{1,21,2} - 20_{0,20,2}$	1.37	185.85	1	+
347.4596300	CH_3CHO	$18_{7,12,3} - 17_{7,11,3}$	2.59*	439.79	B	+
347.4735609	C_2H_5OH	$20_{5,16,1} - 19_{5,15,1}$	1.48	267.08	1	-
347.4783957	CH_3OCHO-E	$27_{1,26} - 26_{1,25}$	1.84	247.25	1	-
347.4939937	CH_3OCHO-A	$27_{5,22} - 26_{5,21}$	1.84	247.25	1	+
347.5194000	CH_3CHO	$18_{3,16,0} - 17_{3,15,0}$	2.35	178.75	B	+
347.5275021	CH_3CHO	$14_{2,13,6} - 14_{1,14,6}$	1.21	483.43	B	-
347.5324834	CH_3CHO	$19_{0,19,5} - 18_{1,18,4}$	1.54	376.56	B	-
347.5635800	CH_3CHO	$18_{3,16,1} - 17_{3,15,1}$	2.34	178.71	B	-
347.5686348	$(CH_3)_2CO$	$31_{22,10,0} - 30_{23,7,0}$	1.79	415.59	A	-
347.5899095	CH_3OCHO-A	$16_{6,10} - 15_{5,11}$	0.43	104.44	1	+
347.6045600	CH_3OCHO-E	$28_{10,18} - 27_{10,17}$	1.81	306.76	1	+
347.6169166	C_2H_5OH	$12_{2,10,1} - 11_{1,11,1}$	-1.39	132.23	1	-|
347.6170100	CH_3OCHO-A	$28_{10,19} - 27_{10,18}$	1.81	306.76	1	-|
347.6283400	CH_3OCHO-E	$28_{10,19} - 27_{10,18}$	1.81	306.76	1	-|
347.6283880	CH_3OCHO-A	$28_{10,18} - 27_{10,17}$	1.81	306.76	1	-|
347.6503726	CH_3CHO	$18_{4,15,0} - 17_{4,14,0}$	2.34	194.51	B	+
347.6661969	CH_3CHO	$18_{6,13,4} - 17_{6,12,4}$	2.30	443.35	B	+

Table A.1. continued.

Frequency	Molecule	Transition	$\log(\mu^2 S)^a$	E_u [K]^b	Flag^c	Plot^d
347.6860359	CH$_3$OCHO-E	$28_{10,18} - 27_{10,18}$	0.05	306.76	A	+
347.7549038	C$_2$H$_5$OH	$20_{4,17,1} - 19_{4,16,1}$	1.49	256.16	A	-|
347.7568500	CH$_3$CHO	$18_{4,15,1} - 17_{4,14,1}$	2.33	194.43	B	-|
347.7675836	CH$_3$OCHO-E	$45_{10,36} - 45_{9,37}$	0.84	629.78	1	+
347.7884000	^{13}CH$_3$OH	$13_{4,9} - 14_{3,11}(E)$	0.57	302.50	1	-
347.7950424	C$_2$H$_5$OH	$38_{2,36,1} - 38_{1,37,1}$	-0.68	681.50	A	-
347.8349955	CH$_3$CHO	$18_{4,14,2} - 17_{4,13,2}$	2.63*	161.11	B	-|
347.8354356	C$_2$H$_5$CN	$42_{9,33} - 43_{7,36}$	-1.12	478.30	A	-|
347.9115075	(CH$_3$)$_2$CO	$35_{0,35,1} - 34_{1,34,1}$	4.15*	270.92	A	-
347.9455996	C$_2$H$_5$CN	$30_{4,26} - 30_{1,29}$	0.00	218.53	1	+
347.9537539	C$_2$H$_5$OH	$14_{3,12,1} - 13_{2,11,1}$	-1.28	159.97	1	+
348.0103300	CH$_3$CHO	$18_{7,12,4} - 17_{7,11,4}$	2.28	471.78	B	+
348.0324330	H$_2$C^{18}O	$5_{2,3} - 4_{2,2}$	1.36	97.50	1	+
348.0448423	C$_2$H$_5$CN	$22_{7,15} - 23_{5,18}$	-1.78	163.24	A	-
348.0500083	CH$_3$OCHO-E	$28_{4,24} - 27_{4,23}$	1.85	266.05	1	-
348.0659670	CH$_3$OCHO-A	$28_{6,23} - 27_{6,22}$	1.85	266.05	1	+
348.0761410	CH$_3$CHO	$18_{8,11,4} - 17_{8,10,4}$	2.26	505.18	B	-
348.0830973	CH$_3$C^{13}CH	$21_1 - 20_1$	1.07	190.99	1	-
348.0875400	CH$_3$CHO	$18_{6,13,3} - 17_{6,12,3}$	2.60*	409.86	B	-
348.1001940	^{13}CH$_3$OH	$11_{0,11} - 10_{1,9}(E)$	0.70	162.36	1	+
348.1174691	^{34}SO$_2$	$19_{4,16} - 19_{3,17}$	1.44	212.60	1	-
348.2115900	CH$_3$CHO	$18_{3,16,3} - 17_{3,15,3}$	2.34	383.20	B	+
348.2290900	CH$_3$CHO	$18_{4,15,4} - 17_{4,14,4}$	2.33	399.64	B	+
348.2605616	C$_2$H$_5$CN	$39_{2,37} - 38_{2,36}$	2.76	343.77	1	+
348.2884900	CH$_3$CHO	$18_{3,15,5} - 17_{3,14,5}$	2.34	385.26	B	+
348.3445240	C$_2$H$_5$CN	$40_{2,39} - 39_{2,38}$	2.77	351.03	A	+
348.3682909	CH$_3$CHO	$20_{0,20,6} - 19_{1,19,6}$	1.60	559.91	B	+
348.3833571	CH$_3$CHO	$24_{5,20,7} - 24_{4,20,8}$	1.28	709.71	B	-
348.3878000	SO$_2$	$24_{2,22} - 23_{3,21}$	1.28	292.73	A	-
348.4268300	HCOOD	$26_{2,24} - 26_{1,25}$	-0.11	386.56	1	+
348.5290690	CH$_3$OCHO-E	$39_{6,34} - 39_{4,36}$	0.94*	406.72	1	-
348.5343647	H$_2$CS	$10_{1,9} - 9_{1,8}$	1.91	105.19	1	-
348.5490239	CH$_3$OCH$_3$	$13_{11,2,0} - 14_{10,5,0}$	0.97*	219.31	A	+
348.5533063	C$_2$H$_5$CN	$40_{1,39} - 39_{1,38}$	2.77	350.99	1	-
348.5607352	CH$_3$CHO	$18_{4,14,2} - 17_{4,14,1}$	0.47	194.47	B	+
348.5741708	CH$_3$CHO	$18_{5,14,3} - 17_{5,13,3}$	2.62*	384.77	B	+
348.5926077	CH$_3$CHO	$19_{0,19,3} - 18_{1,18,3}$	1.49	378.44	B	+
348.6909162	CH$_2$DCN	$20_{1,19} - 19_{1,18}$	2.49	181.14	B	-
348.7201594	C$_2$H$_5$OH	$4_{4,0,1} - 3_{3,0,0}$	0.93*	56.10	1	+
348.7487090	CH$_3$CHO	$18_{3,16,6} - 17_{3,15,6}$	2.34	565.54	B	+
351.1186500	CH$_3$CHO	$18_{1,17,5} - 17_{1,16,5}$	2.35	368.31	B	-
351.1780478	^{33}SO$_2$	$8_{4,4,10} - 8_{3,5,10}$	1.46*	37.92	A	+
351.1955218	D$_2$CO	$6_{5,1} - 5_{5,0}$	1.30*	159.97	1	+
351.2363430	CH$_3$OH	$9_{5,5} - 10_{4,6}(A+)$	0.14	240.50	1	-|
351.2372003	C$_2$H$_5$OH	$20_{6,15,2} - 19_{6,14,2}$	-1.41	221.82	A	-|
351.2412110	HNCO	$16_{4,12,15} - 15_{4,11,15}$	2.36*	801.97	A	-
351.2572233	SO$_2$	$5_{3,3} - 4_{2,2}$	0.86	35.89	1	+
351.4171451	HNCO	$16_{3,14,15} - 15_{3,13,15}$	2.38*	499.10	A	+
351.4649831	O^{13}CS	$29 - 28$	1.17	253.05	1	+
351.4897729	D$_2$CO	$6_{4,2} - 5_{4,1}$	1.86*	111.51	1	-
351.4923762	C$_2$H$_5$OH	$37_{5,32,0} - 36_{6,30,1}$	0.91	678.95	1	-
351.5172503	CH$_3$OCHO-E	$29_{3,26} - 28_{3,25}$	1.87	274.21	B	-
351.5314432	C$_2$H$_5$CN	$16_{5,12} - 15_{4,11}$	0.98	86.27	1	-
351.5378152	HNCO	$16_{2,15,15} - 15_{2,14,15}$	2.08*	282.77	1	-
351.5424856	^{33}SO$_2$	$6_{4,2,5} - 6_{3,3,5}$	1.40*	24.12	A	-
351.5482880	HN^{13}CO	$16_{2,15,15} - 15_{2,14,15}$	2.08*	282.35	A	-
351.5519350	HNCO	$16_{2,14,15} - 15_{2,13,15}$	2.08*	282.77	A	-
351.5745100	CH$_3$CHO	$13_{2,12,0} - 12_{1,11,0}$	1.04	93.01	B	-
351.5889840	CH$_3$CHO	$6_{3,3,0} - 5_{2,4,0}$	0.83	39.81	B	-
351.6286600	(CH$_3$)$_2$CO	$43_{3,40,0} - 43_{2,41,0}$	2.69*	472.86	A	-
351.6334579	HNCO	$16_{0,16,15} - 15_{0,15,15}$	2.09*	109.70	A	-|
351.6352310	^{33}SO$_2$	$5_{4,2,4} - 5_{3,3,4}$	1.25*	18.60	A	-|
351.6428731	HN^{13}CO	$16_{0,16,15} - 15_{0,15,15}$	2.09*	109.71	A	-
351.6962430	CH$_3$OCHO-E	$19_{2,17} - 19_{2,18}$	-1.65	126.22	B	-
351.7686450	H$_2$CO	$5_{1,5} - 4_{1,4}$	1.89	62.45	1	+

Table A.1. continued.

Frequency	Molecule	Transition	$\log(\mu^2 S)^a$	E_u [K]^b	Flag^c	Plot^d
351.8738732	SO_2	$14_{4,10} - 14_{3,11}$	1.29	135.87	A	+
351.9947623	HNCO	$23_{1,23,24} - 24_{0,24,24}$	1.80*	299.51	A	+
352.2321000	CH_3CHO	$19_{1,19,1} - 18_{1,18,1}$	2.38	172.12	B	-
352.2436863	D_2CO	$6_{3,3} - 5_{3,2}$	1.39	107.60	B	+
352.2511849	CH_3CHO	$19_{1,19,0} - 18_{1,18,0}$	2.38	172.05	B	-
352.2554824	$HNC^{18}O$	$17_{1,17,16} - 16_{1,16,16}$	2.12*	161.65	A	+
352.5995703	OCS	$29 - 28$	1.17	253.87	1	+
352.8978650	HNCO	$16_{1,15,15} - 15_{1,14,15}$	2.09*	153.37	A	+
352.9200176	CH_3OCHO-E	$31_{5,27} - 30_{5,26}$	2.21*	252.55	1	-

Notes. This table is also available in electronic form at `http://www.nbi.dk/$\sim$jeskj/sma-iras16293.html`. $^{(a)}$ Catalog line strength for transition. "$*$" indicates multiple hyperfine components from the catalog entry added together. $^{(b)}$ Energy of upper level for transition. $^{(c)}$ Flag describing identification of line: "1" indicates transition detected toward both components, "A" transition only detected to IRAS 16293A and "B" transition only detected toward IRAS 16293B. Transitions that are close in frequency / blended are grouped with the vertical lines in this column. $^{(d)}$ "+" indicates transitions included in the maps in Fig. 12–15 for specific species.